TECHNISCHE UNIVERSITÄT WIEN
Vienna University of Technology

Master Thesis

Controlled trapping and detection of magnetic microparticles

Submitted at the Faculty of Electrical Engineering, Vienna University of Technology in partial fulfillment of the requirements for the degree of Master of Sciences (Diplomingenieur)

under supervision of

Ao.Univ.Prof. Dr. Franz Keplinger
Dr. Ioanna Giouroudi
Dipl.-Ing. Georgios Kokkinis

by

Martin Stipsitz, BSc.
Matr.Nr. 0825709
Am Harrasbach 10, 2223 Martinsdorf

Wien, September 11, 2014 _____

Abstract

In this thesis a microfluidic device for manipulating and detecting magnetic particles (MPs) suspended in a microfluidic channel is presented. Current carrying conductors are used, to move the MPs to a giant magnetoresistance (GMR) sensor, where they are detected. MPs can be functionalised by modifying their surface, to enable them to chemically bind to a biological cell. Thus the device could be integrated in a lab-on-a-chip (LOC), to indirectly detect biological cells.

Calculations concerning the magnetic field of the conductors and the magnetic field of the MPs have been performed to determine the optimal position of the GMR sensor and estimate the output voltage of the system. Two different chip designs have been fabricated. One with a small GMR sensor to detect single MPs and another one, which attracts MPs from a wide area to a bigger GMR sensor, to detect low concentrations of MPs.

Several experiments, in which different MPs have been successfully detected, have been conducted as a proof of concept.

Kurzfassung

In dieser Diplomarbeit wird ein Chip zum Steuern und Detektieren von magnetischen Partikeln (MPs) innerhalb eines mikrofluidischen Kanals vorgestellt. Stromführende Leiterbahnen werden verwendet, um die MPs zu einem giant magnetorestance (GMR) Sensor zu transportieren, wo sie detektiert werden. MPs können durch funktionalisiert werden indem man ihre Oberfläche so verändert, dass sie sich chemisch an bestimmten biologischen Zellen binden. Der Chip könnte daher in ein Lab-on-a-chip (LOC) integriert werden, um indirekt biologische Zellen zu detektieren.

Es wurden Berechnungen zur Bestimmung des Magnetfeldes der Leiterbahnen und der MPs durchgeführt um die optimale Position des GMR Sensors zu bestimmen und die Ausgangsspannung des Systems abzuschätzen. Zwei verschiedene Chipdesigns wurden produziert. Eines mit einem kleinen GMR Sensor um einzelne Partikel zu detektieren und eines, welches MPs von einem großen Gebiet zu einem größeren GMR Sensor transportiert, um niedrige Konzentrationen von MPs zu detektieren.

Mehrere Experimente, in denen verschiedene MPs erfolgreich detektiert wurden, wurden durchgeführt.

Acknowledgment

I am using this opportunity to express my gratitude to everyone who supported me throughout the course of my thesis. I am thankful for their aspiring guidance, invaluably constructive criticism and friendly advice during the work. I am sincerely grateful to them for sharing their truthful and illuminating views on a number of issues related to the thesis.

Foremost, I would like to express my sincere gratitude to Ao.Univ.Prof. Dr. Franz Keplinger, Dr. Ioanna Giouroudi and Dipl.-Ing. Georgios Kokkinis for their support and guidance throughout my work.

I thank my parents for supporting me throughout all my studies at University.

Finally, I want to thank everybody who contributed to the success of this master thesis with their technical or personal support.

Contents

Nomenclature

CIP	Current in plane
CPP	Current perpendicular to plane
Cr	Chromium
DC	Direct current
DI-water	Deionised water
Fe	Iron
GMR	Giant magnetoresistance
GPIB	General Purpose Interface Bus
Ir	Iridium
LOC	Lab-on-a-chip
MBE	Molecular beam epitaxy
MgO	Magnesium oxide
Mn	Manganese
MP	Magnetic particle
Ni	Nickel
PDMS	Polydimethylsiloxane
Ru	Ruthenium
SAF	Synthetic antiferromagnet
Si	Silicon
SiO_2	Silicon dioxide
USB	Universal Serial Bus

1. Introduction

Since the 1990ies, the interest in lab-on-a-chip (LOC) devices for clinical diagnosis has grown rapidly [1]. In an LOC device several laboratory functions are integrated on a single chip with microfluidic channels. Thus only a minimum of fluids is needed, leading to a tremendous economic advantage. Because of diffusion lengths in the order of micrometers, LOCs show comparatively low reaction times and their large surface-to-volume ratio offers an intrinsic compatibility to surface-based assays.

A common approach to detecting biological molecules is to attach to the target molecule a label that produces an externally observable signal [2]. Traditionally, this is accomplished using biomolecular recognition between the target molecule and a specific receptor (e.g. an antibody) that is tagged with the label. The label may be a radioisotope, enzyme, fluorescent molecule or charged molecule, for example. Methods to sense the attached labels have been developed based on a variety of transduction mechanisms, including optical, electrical, electrochemical, thermal and piezoelectric means.

Recently magnetic particles have been developed as labels for biosensing [2]. Magnetic labels have several advantages over other labels. The magnetic properties of the particles are very stable over time, in particular because this property is not affected by reagent chemistry or subject to photo-bleaching. From a detection standpoint, there is not usually a significant magnetic background present in a biomolecular sample. Furthermore, magnetic fields are not screened by aqueous reagents or biomaterials. In addition, current carrying conductors or magnets may be used to remotely manipulate the magnetic particles by a magnetic field. Finally, a number of sensitive magnetic field detection devices have been developed that are suitable for biosensing applications, including giant magnetoresistive (GMR) sensors, inductive sensors, superconducting quantum interference devices (SQUIDs), anisotropic magnetoresistive (AMR) rings and miniature Hall sensors.

GMR sensors consist of thin-film metal multilayers and change their resistance in response to a magnetic field [3]. GMR sensors can be patterned with photolithographic technology, which allows a sensor size in the nm region. This fact and their high sensitivity makes them ideal for detection of MPs. GMR sensors are commercially used for reading magnetic tapes or disks, for hand-held magnetic field sensors and for position transducers.

In this thesis two microchips are presented, which are designed to manipulate and trap magnetic particles (MPs) by current carrying conductors and detect them with a GMR

sensor in a microfluidic channel.

2. Theory

In this chapter the necessary theory about superparamagnetic particles, giant magnetoresistance (GMR) and microfluidics is explained.

2.1. Superparamagnetism

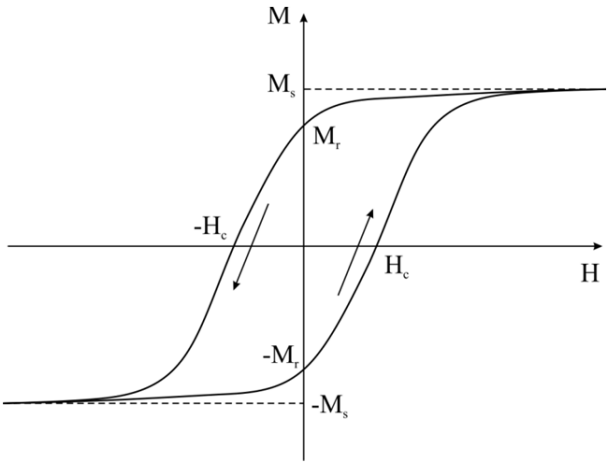

Figure 2.1.: Typical magnetisation curve (magnetisation M as a function of the magnetic field H) of a ferromagnetic material showing hysteresis. Several magnetic parameters are shown: saturation magnetisation M_s, remanent magnetisation M_r and coercivity H_c [4]

The magnetisation curve (magnetisation M as a function of the magnetic field H) of a material can be used to describe its magnetic behaviour. Figure 2.1 illustrates a magnetisation curve of a ferromagnetic material showing the typical hysteresis loop. As the external magnetic field increases, the spins in the material will at some point all align with the external magnetic field and the magnetisation of the material reaches its maximum value, the saturation magnetisation M_s. When the applied magnetic field decreases, the spins will cease to be aligned with the field, hence the total magnetisation of the material decreases. When the external magnetic field decreases to zero, a ferromagnetic material

retains a considerable degree of magnetisation, called remanent magnetisation M_r. To bring the magnetisation of the material back to zero, a magnetic field in the negative direction has to be applied. The value of the external field at which the magnetisation becomes zero is called coercive field H_c. If the field is further increased in the negative direction, the material reaches at some point its saturation magnetisation in negative direction. When the external field decreases, reaches zero and is increased in positive direction, the hysteresis loop is completed [4].

All materials react to magnetic fields to some extent. They can be classified by their volumetric magnetic susceptibility χ, which describes the relation between the magnetisation M induced in a material by the magnetic field H:

$$M = \chi H \tag{2.1}$$

Most materials display little magnetism in the presence of an external field. These materials are classified either as paramagnets ($\chi = 10^{-6}$ to 10^{-1}), or diamagnets ($\chi = -10^{-6}$ to -10^{-3}). However, some materials exhibit ordered magnetic states and are magnetic even without a field applied; these are classified as ferromagnets, ferrimagnets and antiferromagnets, where the prefix refers to the nature of the coupling interaction between the electrons within the material. Large spontaneous magnetisations may arise because of this coupling, which leads to much larger χ and M values. The susceptibility in ordered materials depends on the applied magnetic field, which is the reason for the characteristic sigmoidal shape of the magnetisation curve, with M reaching a saturation value at high values of H. Hysteresis loops can be observed in ferromagnetic and ferrimagnetic materials [4] (Figure 2.1).

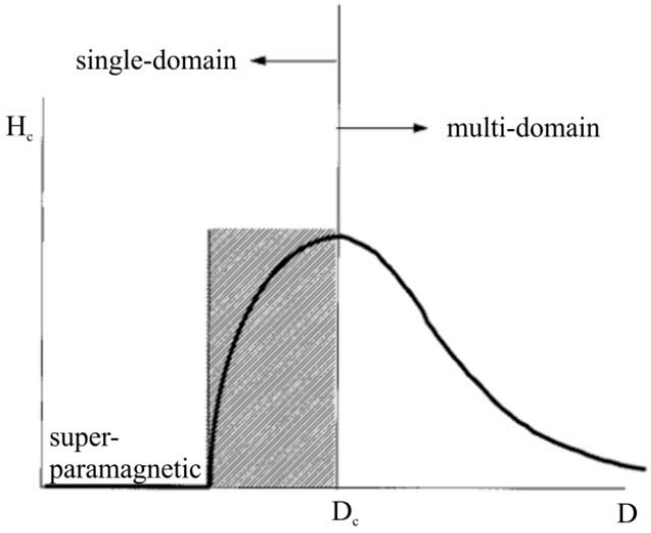

Figure 2.2.: Relation between the coercitivity and particle sizes in particle systems [4]

A group of spins with the same direction of magnetic moments that act cooperatively in the magnetisation procedure is called a domain. Domains are separated by domain walls, which have a characteristic width and energy associated with their formation and existence. Domain wall movement is a primary means of reversing magnetisation. Figure 2.2 qualitatively shows the relation between the coercitivity and particle sizes in particle systems [4]. In large particles (micron sized or even bigger), energetic considerations favour the formation of domain walls, thus giving rise to a multi-domain structure. The magnetisation of such particles is realised by domain wall movement. As the particle size decreases and approaches a critical particle diameter D_c, the formation of domain walls becomes energetically unfavourable and the particles consist of single-domains. Magnetisation changes in single-domain particles are realized through the rotation of magnetic domains. As the particle size is much smaller than D_c, the spins in the particles are affected by thermal fluctuations and such particles are called superparamagnetic particles [4]. The magnetisation curve of superparamagnetic particles is anhysteretic, but still sigmoidal [?]. This means that they show no remanent magnetisation after removal of an external magnetic field and it is possible to "turn off" the magnetisation of superparamagnetic particles by removing the magnetic field. Figure 2.3 illustrates magnetisation curves for diamagnetic, paramagnetic and superparamagnetic materials.

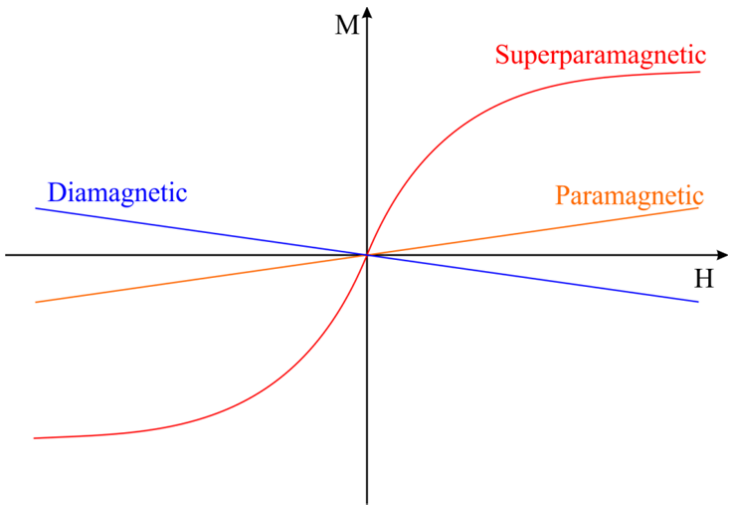

Figure 2.3.: Magnetisation curves for diamagnetic, paramagnetic and superparamagnetic materials [4]

2.2. Magnetic force on a magnetic particle (MP)

A single MP can be approximated by a point like magnetic dipole which has a magnetic moment m:

$$\vec{m} = V_P \vec{M} \tag{2.2}$$

where V_P is the particle volume and $\vec{M}$ is the magnetisation. In the case of a superparamagnetic microparticle the magnetisation can be written as:

$$\vec{M} = \Delta\chi \vec{H} \tag{2.3}$$

where $\Delta\chi = \chi_P - \chi_{fluid}$ is the volumetric magnetic susceptibility difference between the particle (χ_P) and the surrounding fluid (χ_{fluid}) and $\vec{H}$ is the magnetic field. The magnetic force experienced by the superparamagnetic MP is given by

$$\vec{F}_m = (\vec{m} \cdot \nabla)\vec{B} \tag{2.4}$$

where $\Delta \cdot \vec{B}$ is the gradient of the magnetic field. When combining equations (2.2) to (2.4) and using the relation $\vec{B} = \mu_0 \vec{H}$, it becomes apparent that the magnetic force acting on the superparamagnetic MP is proportional to the magnetic flux density $\vec{B}$, the gradient of the magnetic field $\nabla \cdot \vec{B}$, the particle volume V_P and the difference in magnetic susceptibility between the fluid and the MP $\Delta\chi$ [5]. It is given by equation (2.5):

$$\vec{F}_m = \frac{V_P \Delta_\chi}{\mu_0}(\vec{B} \cdot \nabla)\vec{B} \tag{2.5}$$

Assuming that there are no time-varying electric fields or currents, the Maxwell equation $\Delta \times \vec{B} = 0$ can be used. If this equation is applied to the mathematical identity

$$\Delta(\vec{B} \cdot \vec{B}) = 2(\vec{B} \cdot \Delta)\vec{B} + 2\vec{B} \tag{2.6}$$

the following identity is obtained:

$$\frac{1}{2}\Delta(\vec{B} \cdot \vec{B}) = (\vec{B} \cdot \nabla)\vec{B} \tag{2.7}$$

and equation (2.5) can be written as:

$$\vec{F}_m = \frac{V_P \Delta_\chi}{\mu_0} \vec{\nabla} \vec{B}^2 \tag{2.8}$$

2.3. Giant Magnetoresistance

The Giant magnetoresistance (GMR) [6] effect is observable in structures of thin layers with ferromagnetic and nonmagnetic materials. Those structures show a strong dependence of the electrical resistance to the magnetic field. Already at it's discovery in 1988 this effect showed ten times higher resistance changes than the anisotropic magnetoresistance effect. However, there were strong magnetic fields of about 150kA/m and low temperatures needed. The experiments were carried out at the boiling point of liquid Helium (4.2K). The GMR-material consisted of ferromagnetic Fe-layers and antiferromagnetic Cr-Layers, which were produced by molecular beam epitaxy (MBE), with a thickness of a few nanometers (figure 2.4, left).

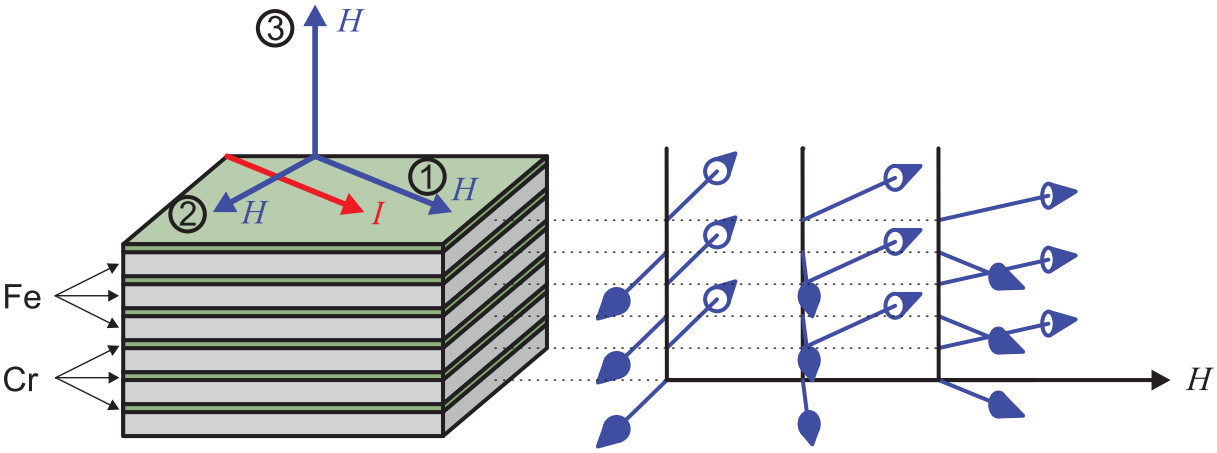

Figure 2.4.: Fe/Cr-Sandwich. The current flows in the plane of the layers (CIP current in plane), the numbers indicate the different directions in comparison to the current-direction. The right picture shows the magnetisation process in the antiferromagnetic Fe-layers at increasing field strength.

Without the Cr-layers the Fe-layers would be coupled ferromagneticaly. The magnetisation would point in the same direction for the whole structure. But due to the Cr-layers, the Fe-layers are coupled antiferromagnetically due to the RKKY-interaction. Thus the system is hard to saturate. The coupling depends on the thickness of the Cr-layers. If the

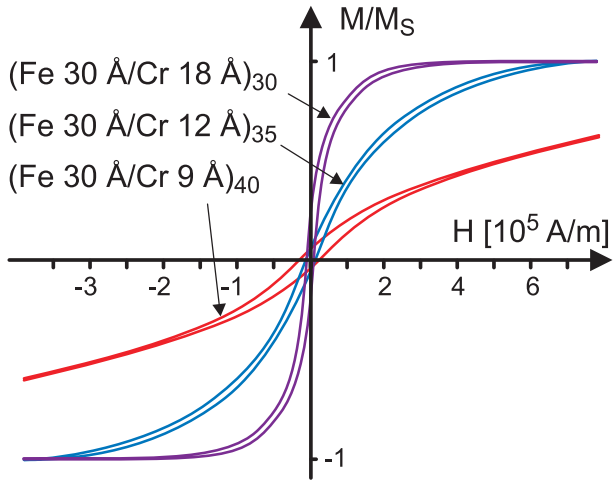

Figure 2.5.: Hysteresis loop for a Fe/Cr-superlattice with different thicknesses of the Cr-layers and equal overall thickness. The index indicates the number of double layers. Lattice constant $a_{Cr} \approx 3\mathring{A}$, field direction [110], $T = 4,2$K. [6]

Cr-layers are thicker, the coupling of the Fe-layers gets weaker and the system is easier to saturate.

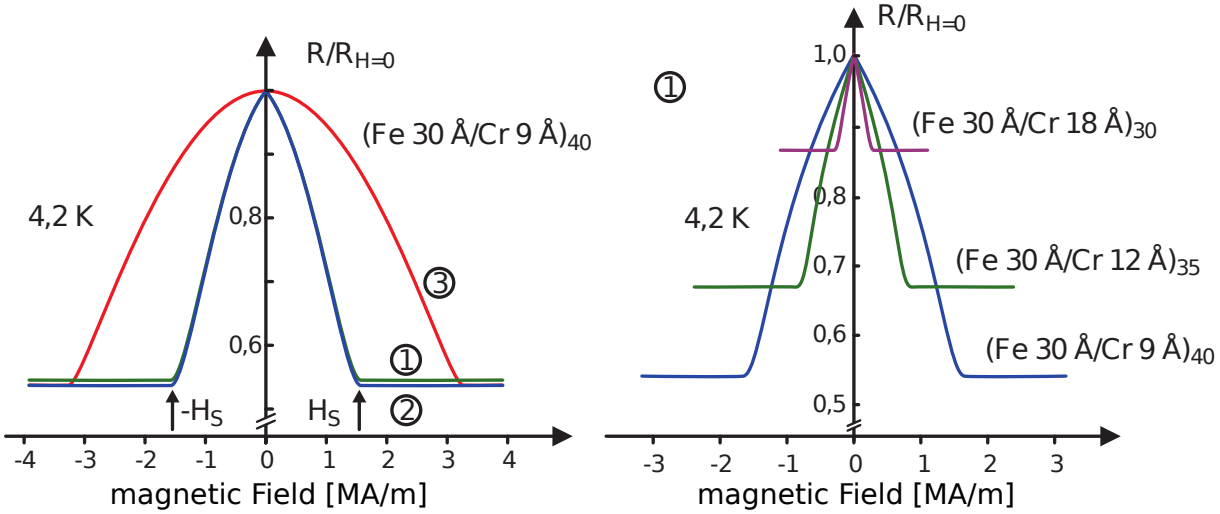

Figure 2.6.: Magnetoresistance: Left figure: [Fe $30\mathring{A}$/(Cr 9 $\mathring{A}$)]$_{40}$ superlattice at 4.2K along the direction of the current ①, in the layer perpendicular to the current direction ② and perpendicular to the layers ③. Right figure: Different Fe/Cr-superlattices, with different Cr-thicknesses. Current and Field in [110]-direction. [6]

The electric resistance of such film systems shows a strong dependency of the magnetic field (figure 2.6). If the Fe-layers are magnetised antiferromagnetically, the resistance is

higher than when the magnetic moments of the layers point in the same direction. The bigger the antiferromagnetic coupling the bigger is the effect. Thus the strongest effect can be observed with three layers of Cr-Atoms ($\approx 9\mathring{A}$).

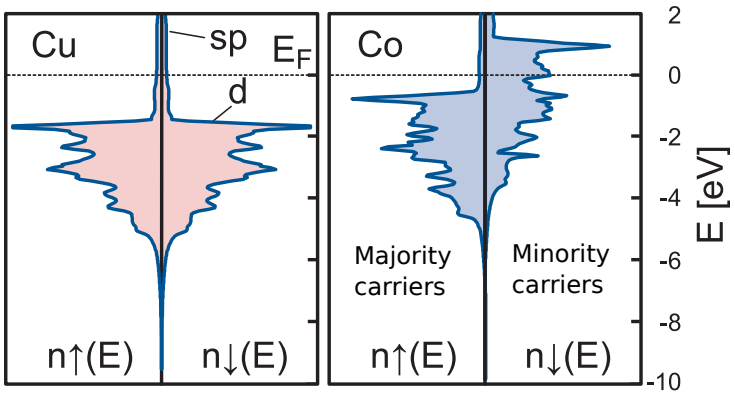

Figure 2.7.: Density of states of diamagnetic copper (left) and ferromagnetic cobalt (right). [6]

Whereas the spin of electrons does not influence the properties of common components, it is responsible for the change of the electrical resistance due to a magnetic field at the GMR-effect. The spin is quantised related to the direction of the magnetic field ($\pm 1/2$). Electrons with the spin pointing in the direction of the magnetic field are called spin-up-electrons, otherwise they are called spin-down-electrons. Those two states are not equivalent in the presence of a magnetic field. Spin-up-electrons are energetically preferred and dominate in a magnetised material. Hence ferromagnetic materials like cobalt, differ significantly from nonmagnetic materials like the diamagnetic copper. Figure 2.7 shows the density of states for copper and cobalt. For copper, which shows no magnetisation, the densities of states for spin-up- and spin-down-electrons are the same. For cobalt the density of states for spin-up-electrons is shifted to a lower level, because of the spontaneous magnetisation of the domains. This does not tell anything about the density of states at the Fermi level $n(E_F)$. Because of the relatively complicated energy dependence of the d-band, the density of states of spin-up-electrons $n_\uparrow$ at the Fermi level can be much lower than the density of states of spin-down-electrons $n_\downarrow$. Because only the electrons close to the Fermi-level take part in transport processes, the current is dominated by the electrons with the higher density of states at the Fermi level [6].

The spin polarisation P describes the degree of which one sort of electrons dominates:

$$P = \frac{n_\uparrow - n_\downarrow}{n_\uparrow + n_\downarrow} \tag{2.9}$$

If there are only spin-up-electrons, then $P = +1$, with pure spin-down-electrons $P = -1$.

In materials like copper without spin polarisation $P = 0$.

If spin-up-electrons travel into a region magnetised in the other direction, they will be spin-down-electrons there and will be scattered more often than before. Thus the electrical resistance is bigger. The effect is only significant because spin-flip-events, scattering events where the spin changes, are very rare. In the easiest model the resistance change for spin-up- and spin-down-electrons is described by the same factor β:

$$\rho_\uparrow = \rho(1-\beta), \quad \rho_\downarrow = \rho(1+\beta) \tag{2.10}$$

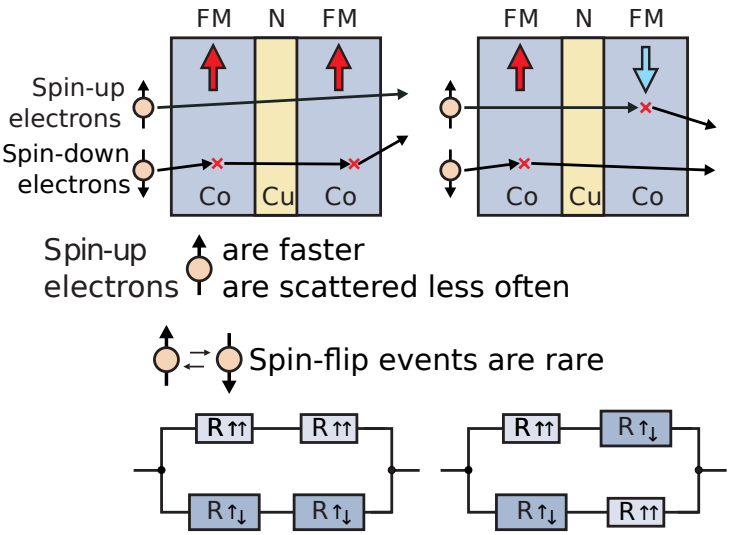

Figure 2.8.: Model for the explanation of the GMR-effect with a structure consisting of ferromagnetic Co and diamagnetic Cu layers. The crosses symbolise the scattering processes. Bigger resistance-symbols represent a bigger resistance-value. [6]

To determine the overall resistance of the layered structure, a parallel circuit is used (figure 2.8), where one branch represents the current of the spin-up-electrons and the other one the current of the spin-down-electrons. The resistance of each layer is represented by a series resistance. So the overall resistance depending on the magnetisation is:

$$\rho_{\uparrow\uparrow} = \rho(1-\beta^2), \quad \rho_{\uparrow\downarrow} = \rho \tag{2.11}$$

In the proposed chips **exchange-biased spin-valve GMR sensors** [7] are used . The layer structures of a spin-valve GMR is shown schematically in figure 2.9. The structure consists essentially of a sandwich structure of two ferromagnetic (F) layers separated by

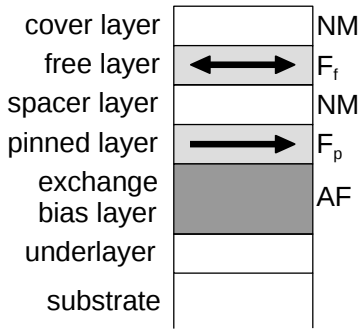

Figure 2.9.: Stack of a spin valve GMR sensor. [7]

a nonmagnetic (NM) spacer layer and an antiferromagnetic (AF) layer that is in contact with one of the F layers. The magnetisation of this F layer, the pinned or reference layer F_p, is held fixed in a certain direction by the strong exchange interaction with the AF layer. Use is made of the exchange anisotropy effect. To a first approximation, the AF/F exchange interaction acts as if a strong local magnetic field, the so-called exchange bias field H_{eb}, acts on the pinned layer. The preferred direction of the pinned layer is determined by the magnetisation direction of the pinned layer during cooling of the system after heating the system to a temperature above the so-called blocking temperature. The blocking temperature T_b, is the temperature above which H_{eb} is zero. [7]

The NM spacer layer serves to magnetically decouple the F-layers. It consists usually of a 2-3 nm Cu layer. Sometimes, the thickness is even less. The thickness should be sufficient to prevent direct ferromagnetic exchange coupling between the layers via pinholes. Even in the absence of pinhole coupling, indirect interlayer exchange coupling (due to a weak magnetic polarisation of the NM layer by the exchange interaction with the F layers) and magnetostatic interactions contribute to a net coupling between the pinned and free F layers. The AF layer can be deposited on the bottom of the structure. Underlayers are frequently used to influence the microstructure of the film (e.g. the grain size, the preferential crystallite orientation and the interface flatness) or to prevent interdiffusion with the substrate. The underlayer may be ferromagnetic. A thin cover layer is often used to protect the structure from corrosion. [7]

When a relatively small magnetic field is applied, the free layer reverses whereas the magnetisation direction of the pinned layer remains unchanged. Figure 2.10a shows a schematic magnetisation curve. The applied magnetic field is parallel to the exchange bias field. By definition, the applied field is positive when its direction is the same as that of the exchange bias field. For sufficiently large fields the free and pinned layers have parallel magnetisations. In a small field interval around the coupling field H_{coupl}, the magnetisation of the free F layer reverses, whereas the magnetisation of the pinned F layer remains fixed. This definition of H_{coupl} implies that it is negative or positive when the coupling is ferromagnetic or antiferromagnetic, respectively. Only upon the application of a large negative field, the exchange bias interaction is overcome and the

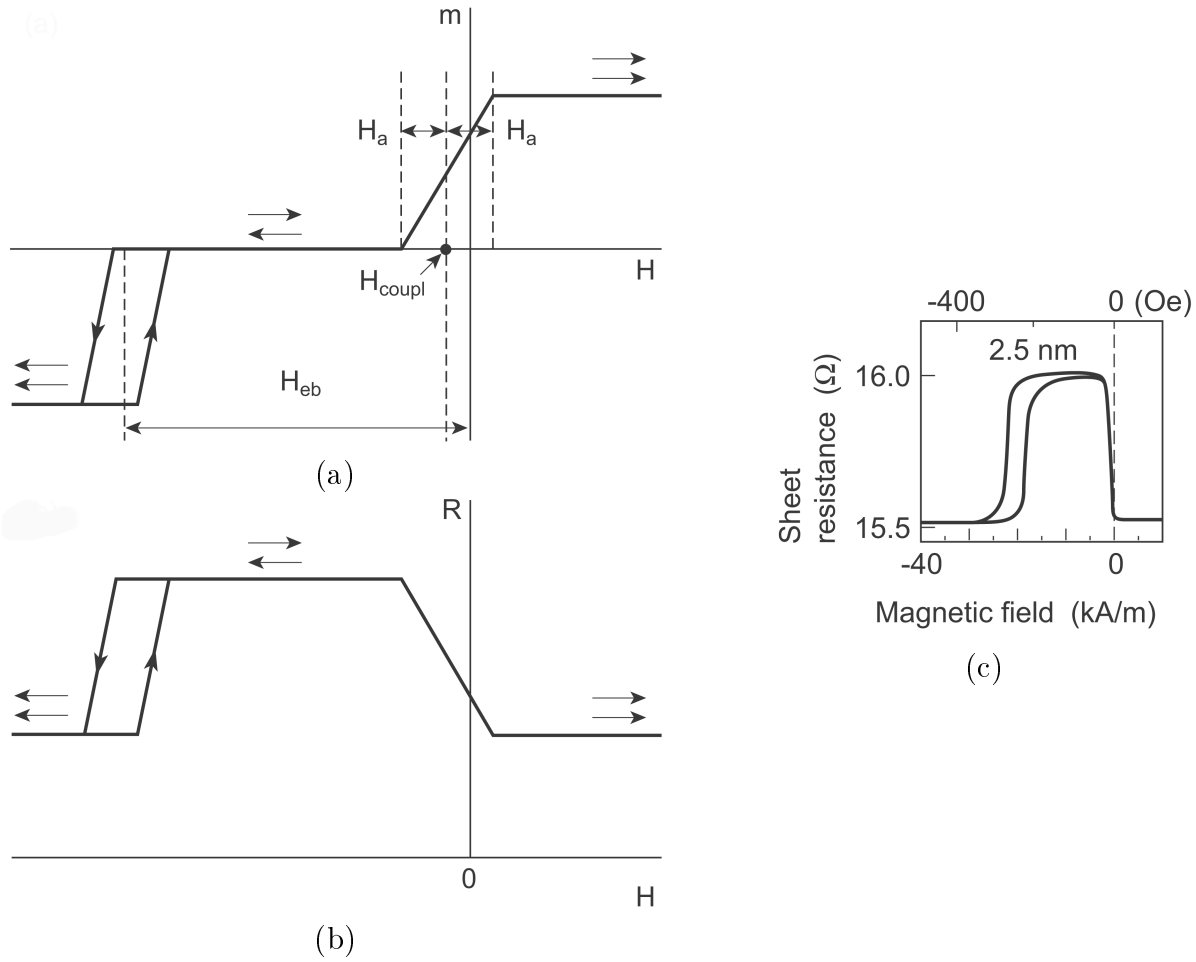

Figure 2.10.: Schematic curves of the magnetic moment (a) and resistance (b) versus the applied magnetic field for a simple SV. The magnetic moments per unit area of the free and pinned layers have been assumed to be equal. The top and bottom arrows indicate the magnetisation directions of the pinned and free layer, respectively. (c) Measured curve of the resistance versus the applied magnetic field. [7]

pinned layer switches too. Assuming ideal conditions $|H_{coupl}| << H_{eb}$, this happens when $H \approx -H_{eb}$. Usually, the switching of the pinned layer is not fully reversible, leading to a certain hysteresis, as indicated in figure 2.10.

GMR sensors can be contacted in CIP-geometry (current in plane) and in CPP-geometry (current perpendicular to plane), like depicted in figure 2.11. In the CIP-geometry the current flows in the plane of the layers. Standard four-point measurements can be carried out easily by applying needle-shaped current and voltage probes directly on the thin-film specimen. For making devices, lithographic patterning is used for defining the multilayer magnetoresistor stripes and low-resistive contact leads. Magnetoresistance studies with CPP-geometries are technically much more demanding than CIP-GMR studies, but have shown GMR ratios up to 300% at cryogenic temperatures. For CPP-geometries it is

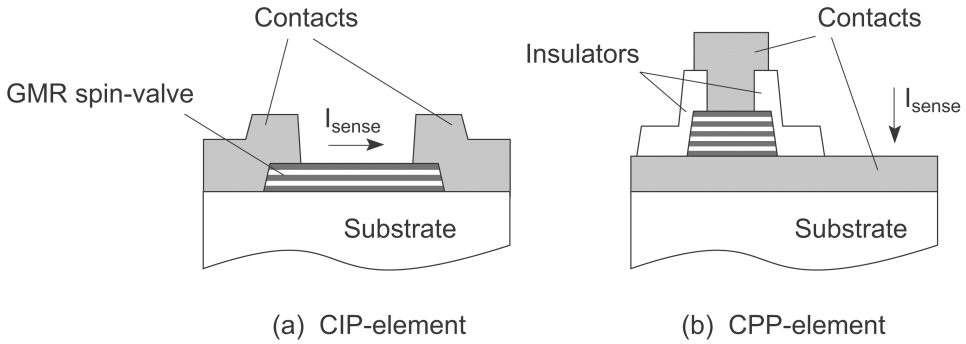

Figure 2.11.: Schematic device structures for measurements of the GMR ratio in (a) the CIP device geometry and (b) the CPP geometry. [7]

necessary to create samples with small cross-sectional areas, in order to obtain a resistance that is not unacceptably low, and to make sure that the contacts function as proper equipotential planes.

2.4. Microfluidics

Microfluidics is a multidisciplinary field intersecting engineering, physics, chemistry, biochemistry, nanotechnology and biotechnology, which deals with small volumes of fluids (μL, nL, pL, fL).

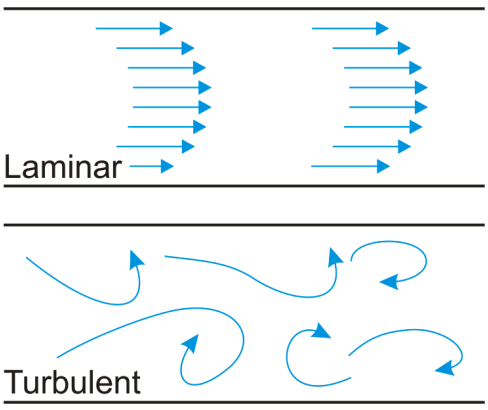

Figure 2.12.: Flow profile of laminar and turbulent flow [8]

The behaviour of such volumes can differ substantially from macroscopic fluids, because at this scale effects dominate, which are negligible in classical fluid mechanics. The behaviour can be determined by the Reynolds number [9], which becomes very low in microfluidic systems and determines the regime of laminar and turbulent flow (figure 2.12).

The Reynolds number describes the ratio between inertial forces and viscous forces in a particular flow and is defined as:

$$Re = \frac{\rho D_h u}{\eta} \tag{2.12}$$

where ρ is the density of the fluid, D_h is the hydraulic diameter, u is the characteristic velocity of the fluid in the channel and η is the dynamic viscosity of the fluid. The transition from laminar to turbulent flow occurs typically in the range of $Re = 1000$ to 2000. Since in microfluidics Re is normally $\ll 1$, the flow is highly laminar. A key consequence of this is that fluids, when side-by-side, do not necessarily mix in the traditional sense, molecular transport between them must often be through diffusion [10].

3. System Design and Implementation

In this chapter two different designs are presented. One design uses circular microrings to attract particles from a wide area towards a GMR sensor and an existing magnetophoresis design, which consists of 9 straight conductors, has been equipped with GMR sensors at the first and the last conductor. In section 3.1 the working principle of the manipulation and detection is explained. In section 3.2 magnetic field calculations for the conductors and the particles are performed to estimate the sensitivity of the system and section 3.3 describes the design considerations.

3.1. Working principle

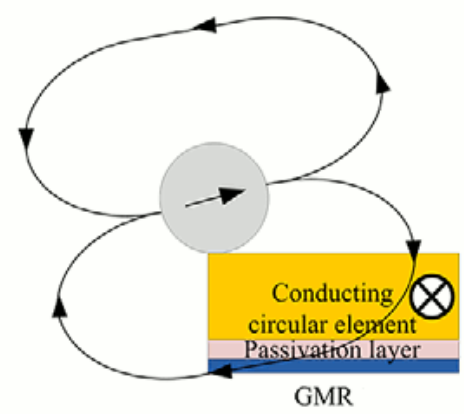

Figure 3.1.: Cross section schematic of the working principle. A magnetic particle lies above a conductor and a GMR sensor.

A schematic of the cross section of a system for detection of magnetic particles is depicted in figure 3.1. The current in a conductor produces a magnetic field, which attracts magnetic particles to a GMR sensor. The stray field of the particles can then be detected by the GMR sensor. Instead of the conductor it would also be possible to use a permanent

magnet. Permanent magnets produce higher magnetic fields but they can not be turned on and off like conductors and can not be integrated on a single chip.

3.2. Calculations

In order to design a GMR sensor to detect MPs, the field produced by an MP must be known. The superparamagnetic MPs only produce a magnetic field, when they are magnetised by the current flowing through the conductor. Thus first the field of the different conductor geometries and then the field produced by the MP must be calculated. Also the position of the MPs can be estimated by the field of the conductors.

The magnetophoresis-chip (second design) consists of long straight conductors with a rectangular cross section. Thus they can be well approximated by an infinite rectangular wire. The microring conductors (first design) will be approximated by filamentary current loops, neglecting the point where the rings are contacted by straight wires.

3.2.1. The field of a infinitely long rectangular wire

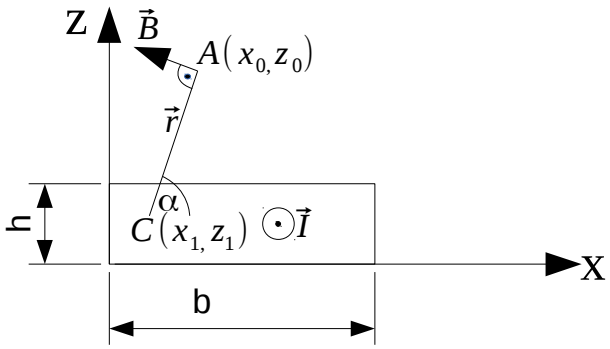

Figure 3.2.: Cross section of a rectangular conductor carrying a uniformly distributed current $\vec{I}$

The magnetic flux density $\vec{B}$ of an infinitely long and infinitely thin straight wire carrying a current $\vec{I}$ can be obtained by the following equation [11]:

$$\vec{B} = \frac{\mu_0 \vec{I}}{2\pi r} \times \vec{e_r} \tag{3.1}$$

where $\vec{r} = r \cdot \vec{e}_r$ is the distance from the wire to the point where $\vec{B}$ is being calculated and μ_0 is the permeability of air.

The field at point A of an infinitesimal small part of the conductor (figure 3.2) at position C can be calculated in the same way:

$$\mathrm{d}\vec{B} = \frac{\mu_0 \vec{J} \cdot \mathrm{d}x_1 \cdot \mathrm{d}z_1}{2\pi r} \times \vec{e}_r = \frac{\mu_0 \vec{J} \cdot \mathrm{d}x_1 \cdot \mathrm{d}z_1}{2\pi r}(\sin\alpha \cdot \vec{e}_x - \cos\alpha \cdot \vec{e}_z) \tag{3.2}$$

where $\vec{J}$ is the current density and $\vec{J} \cdot \mathrm{d}x_1 \cdot \mathrm{d}z_1$ is the current through this infinitesimal small part of the conductor.

With $r = \sqrt{(x_0 - x_1)^2 + (z_0 - z_1)^2}$, $\sin\alpha = \frac{z_0 - z_1}{r}$ and $\cos\alpha = \frac{x_0 - x_1}{r}$, $\vec{B}$ can be calculated by integrating over the area of the conductor:

$$\begin{aligned} \vec{B} &= \int_0^h \int_0^b \frac{\mu_0 \vec{J} \cdot \mathrm{d}x_1 \cdot \mathrm{d}z_1}{2\pi r}(\sin\alpha \cdot \vec{e}_x - \cos\alpha \cdot \vec{e}_z) \\ &= \int_0^h \int_0^b \frac{\mu_0 \vec{J} \cdot \mathrm{d}x_1 \cdot \mathrm{d}z_1}{2\pi\big((x_0 - x_1)^2 + (z_0 - z_1)^2\big)} \cdot \big((z_0 - z_1) \cdot \vec{e}_x - (x_0 - x_1) \cdot \vec{e}_z\big) \end{aligned} \tag{3.3}$$

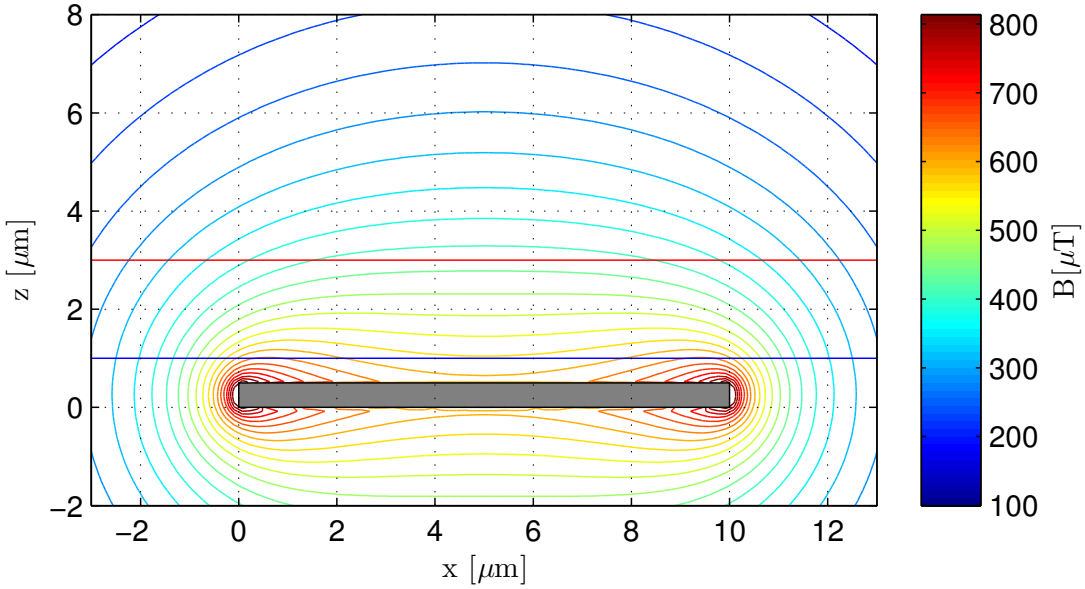

Figure 3.3.: Field of a rectangular wire (grey rectangle) with a height of 500nm and a width of 10 μm, carrying a current of 10mA.

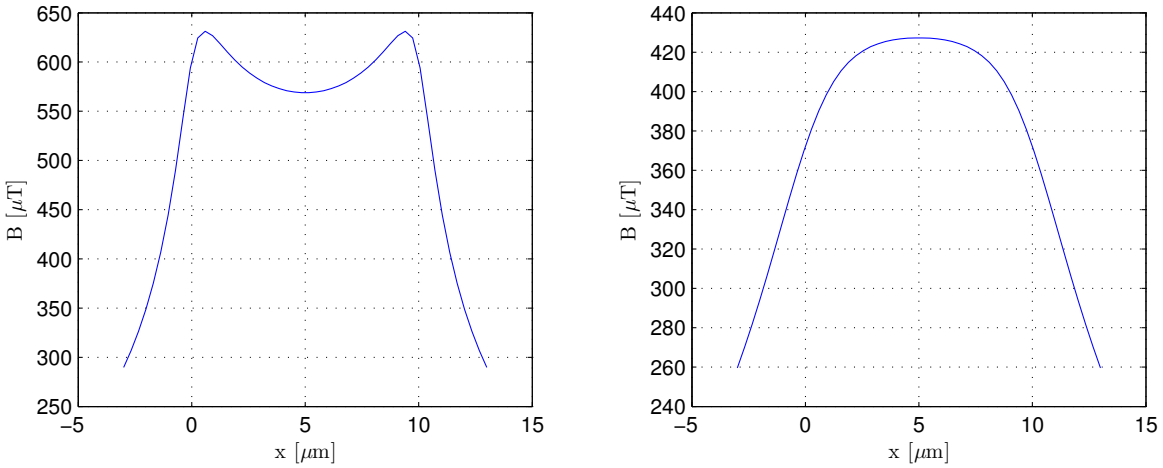

(a) Blue line at $z = 1$ μm

(b) Red line at $z = 3$ μm

Figure 3.4.: Field along the horizontal lines in figure 3.3.

The integration in equation (3.3) was solved numerically with Matlab. The result for a wire with rectangular cross section is depicted in figure 3.3. According to equation (2.5) MPs will move to the maximum of the magnetic field. Since the MPs will be pulled downwards to the surface of the conductor, their position can be estimated by plotting the field along a horizontal line. The field along the two horizontal lines at $z = 1$ μm and $z = 3$ μm is depicted in figure 3.4a and 3.4b. Since the field in figure 3.4a has two maxima at the edges and figure 3.4b has one maximum in the middle, small MPs will be attracted to the edges and big MPs will probably move to the middle of the conductor.

3.2.2. The field of a filamentary current loop

The analytical solution for the field of a current loop can be obtained by using the law of Biot Savart [12]. The following formulas can be used to calculate the magnetic field of the current loop in figure 3.5:

$$B_x = B_0 \frac{1}{\pi\sqrt{Q}} \left[E(k) \frac{1-\alpha^2-\beta^2}{Q-4\alpha} + K(k) \right] \tag{3.4}$$

and

$$B_r = B_0 \frac{\gamma}{\pi\sqrt{Q}} \left[E(k) \frac{1+\alpha^2+\beta^2}{Q-4\alpha} - K(k) \right] \tag{3.5}$$

$$\alpha = \frac{r}{a} \tag{3.6}$$

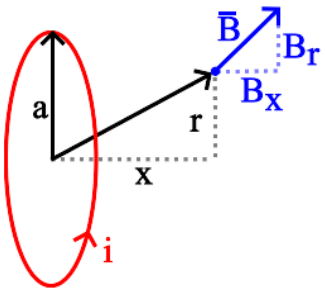

Figure 3.5.: Filamentary current loop

$$\beta = \frac{x}{a} \tag{3.7}$$

$$\gamma = \frac{x}{r} \tag{3.8}$$

$$Q = (1+\alpha)^2 + \beta^2 \tag{3.9}$$

$$k = \sqrt{\frac{4\alpha}{Q}} \tag{3.10}$$

$K(k)$ is the complete elliptical integral of first kind and $E(k)$ is the complete elliptical integral of second kind. These elliptical integrals can only be solved numerically.
$B_0 = i\mu_0/(2a)$ is the magnetic flux density in the center of a current loop.

3.2.3. Distribution of the current in a conductive arc

The current in the microrings will not be uniformly distributed. Current flowing closer to the center of the microrings will observe a lower resistance, than current flowing near the outer border. Thus the current density will be higher on the inner side than on the outer side. Neglecting the disturbance at the contacts of the microrings, the current distribution can be calculated from the conductive arc in figure 3.6. The current lines are supposed to be half circular like the arc itself. With these assumptions the electric field E can be expressed by:

$$E(\rho) = \frac{U}{\rho\pi} \tag{3.11}$$

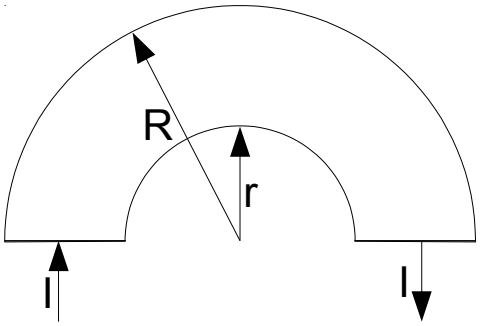

Figure 3.6.: Conducting arc with a current I

where ρ is the radial coordinate and U is the voltage applied to the arc. With the conductivity γ the current density is given by:

$$J(\rho) = \gamma E(\rho) = \gamma \frac{U}{\rho\pi} \tag{3.12}$$

With the thickness of the arc h, the total current I can be calculated by integrating over the cross section area of the arc:

$$I = h \int_r^R J \,\mathrm{d}\rho = h \int_r^R \gamma \frac{U}{\rho\pi} \,\mathrm{d}\rho = h\gamma \frac{U}{\pi} (\ln R - \ln r) \tag{3.13}$$

Equation (3.13) can be rearranged to express the voltage U:

$$U = \frac{I}{h\gamma} \cdot \frac{\pi}{\ln R - \ln r} \tag{3.14}$$

Inserting (3.14) into (3.12) gives the current distribution in the arc for a given current I:

$$J(\rho) = \frac{I}{h\rho} \cdot \frac{\pi}{\ln R - \ln r} \tag{3.15}$$

3.2.4. The field of a microring

From equation (3.4) and (3.5) we know that the magnetic field $\vec{B}$ at point $A(\rho_0, z_0)$ (figure 3.7) originating from a filamentary current loop at point $C(\rho_1, z_1)$ is a function of ρ_0, ρ_1, $(z_0 - z_1)$ and I_{loop}, where I_{loop} is the current of the filamentary current loop. Thus the magnetic field of a rectangular current loop can be obtained by replacing I_{loop} with

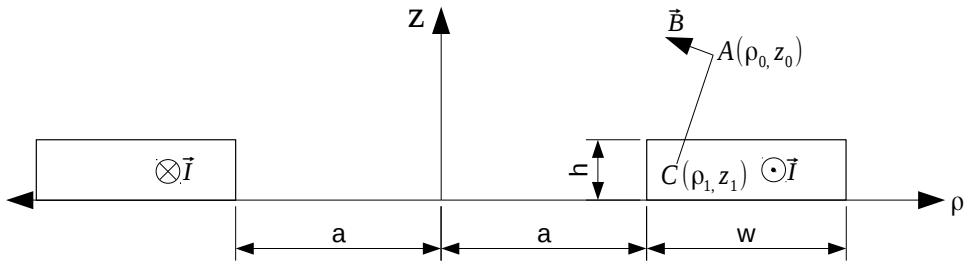

Figure 3.7.: Cross section of the microring

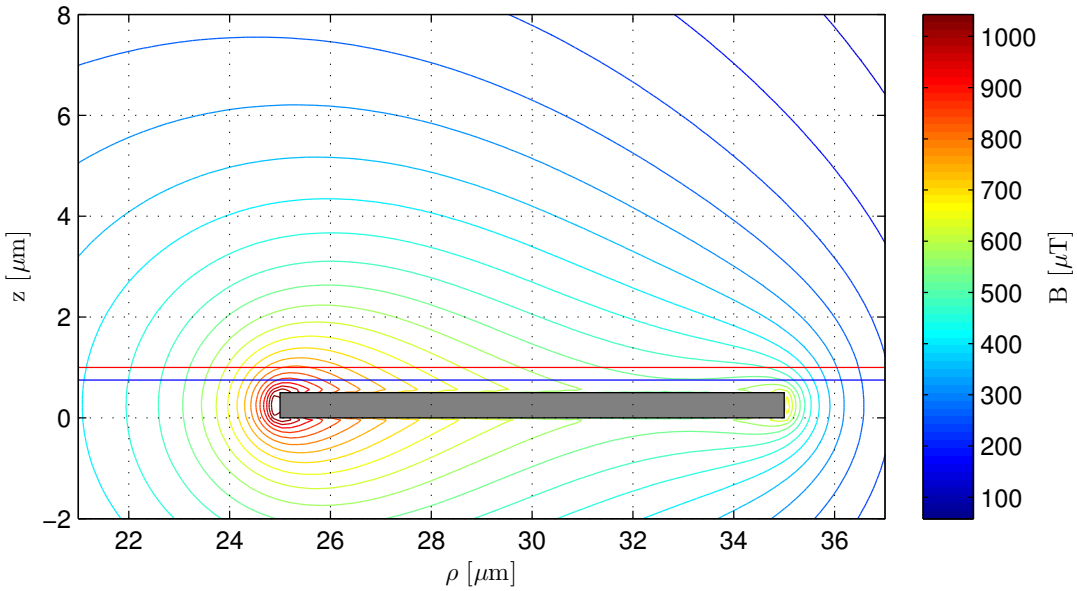

Figure 3.8.: Field of a rectangular microring with 10mA current

the current density J and integrating the function over the height h and the width w of the conductor:

$$\vec{B} = \int_0^h \int_a^{a+w} \vec{f}\left(\rho_0, \rho_1, z_0 - z_1, J\left(\rho_1\right)\right) \mathrm{d}\rho_1 \mathrm{d}z_1 \tag{3.16}$$

where $J(\rho_1)$ is given by equation (3.15).

This integral was solved numerically with Matlab. The result for a microring with rectangular cross section is depicted in figure 3.8. According to equation 2.5 MPs will move to the maximum of the magnetic field. Since the MPs will be pulled downwards to the surface of the conductor, their position is determined in the vertical direction and can be estimated by plotting the field along a horizontal line. The field along the two horizontal

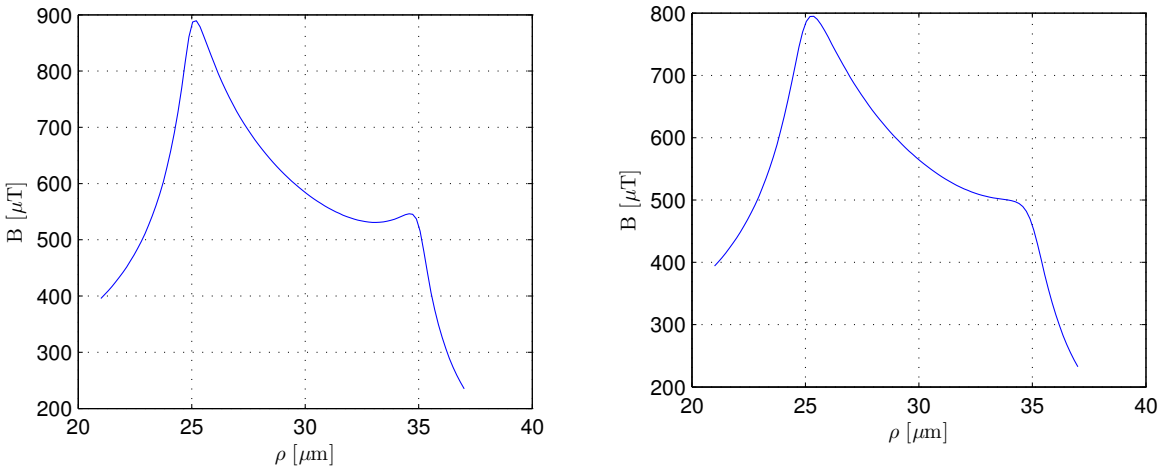

(a) Blue line at $z = 0.75$ μm

(b) Red line at $z = 1$ μm

Figure 3.9.: Field along the horizontal lines in figure 3.8.

lines at $z = 0.75$ μm and $z = 1$ μm is depicted in figure 3.9b and 3.9a. Since the field in figure 3.9a has one maximum at the inner edge of the microring, MPs will be attracted to the inner edge. MPs with a diameter smaller than 0.5 μm could also get stuck at the outer edge of the microring (assuming, that there is no passivation layer above the conductor), since there is also a local maximum in figure 3.9b at the outer edge.

3.2.5. The field of one MP at the GMR sensor

The MPs, which are attracted to the surface of the conductor, will align to the field of the conductor like depicted in figure 3.10a. They are magnetised by the magnetic field of the conductor and produce their own stray field. For the calculation a particle with a diameter of $d = 2.8$ μm and a susceptibility of $\chi = 1.0$ was used.

Because the MP is big compared to the other distances, it can not be approximated by a single dipole. So for the calculation of the magnetic field the 3-dimensional MP was split into small cubes like depicted in figure 3.10b. For each cube the magnetic moment $\vec{m}$ was calculated with the susceptibility χ, the magnetic field of the microring conductor $\vec{H}$ (determined in section 3.2.4), the volume of the a cube V and the side length of the cube a by the following equation:

$$\vec{m} = \chi \vec{H} V = \chi \vec{H} a^3 \tag{3.17}$$

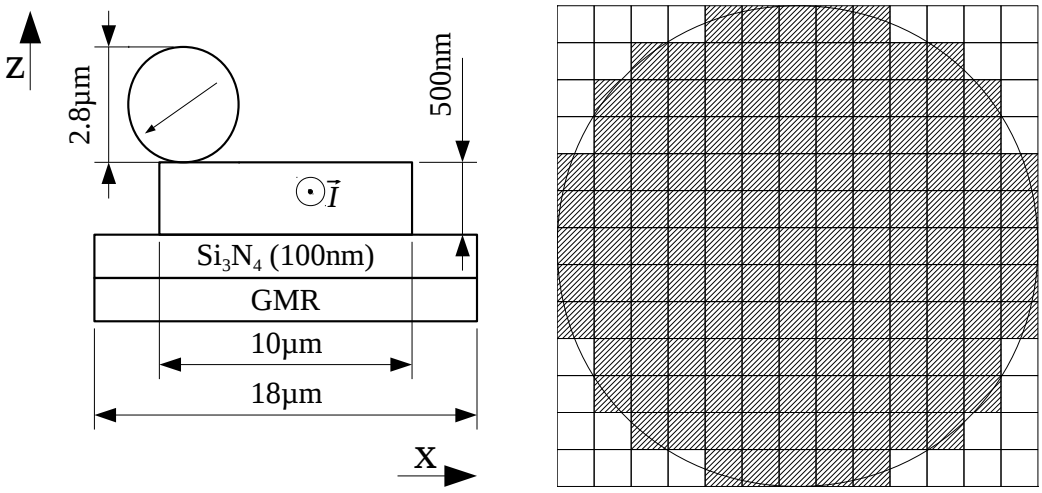

(a) (b)

Figure 3.10.: (a) Position of the MP above the GMR sensor (for the microring-chip). (b) discretisation of the particle with cubes.

To calculate the field of one cube, the formula for the field of a magnetic dipole was used:

$$\vec{B}(\vec{r}) = \frac{\mu_0}{4\pi} \frac{3\vec{r}(\vec{m}\cdot\vec{r}) - \vec{m}r^2}{r^5} \tag{3.18}$$

The field from each cube at the GMR sensor was calculated and summed up to get the field generated from the whole particle. Since the field of the particle decreases very fast with distance, only the field at the GMR sensor in close proximity to the particle was calculated (figure 3.11a) and the rest was neglected. From this result the average field B_{mean} in x-direction (sensitive direction of the GMR sensor) over the whole GMR sensor can be calculated. All of this was performed with several loops using Matlab. The geometry for the calculation is shown in figure 3.11b, where the particle is placed at the most probable position determined in section 3.2.4. For a current through the conductor of 20 mA the result is:

$$B_{mean} = 272 \text{ nT} \tag{3.19}$$

In contrast to the magnetophoresis-chip for the microring-chip also the angle α of the particle in figure 3.12 must be taken into account. The value previously calculated is the field from a particle, which is placed at the x-axis in figure 3.12. If the particle lies at an angle α to the x-axis, the field from the particle in x-direction decreases with $\cos(\alpha)$. To take this into account the average decrease was calculated for a position from 0 to 57° by

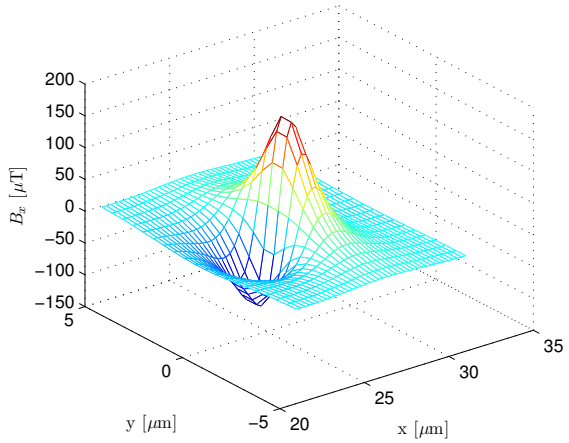

(a) Field in x-direction at the GMR sensor generated by one particle with a current of 20mA through the rectangular conductor.

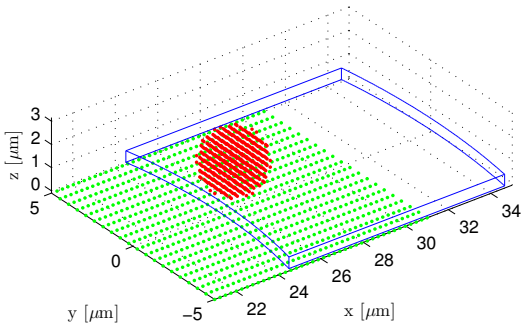

(b) Exact geometry of the simulation with the particle (red), conductor (blue) and GMR sensor (green). The particle and a part of the GMR sensor are drawn by small dots representing the discretisation.

Figure 3.11.: Calculation result and geometry of the microring-chip

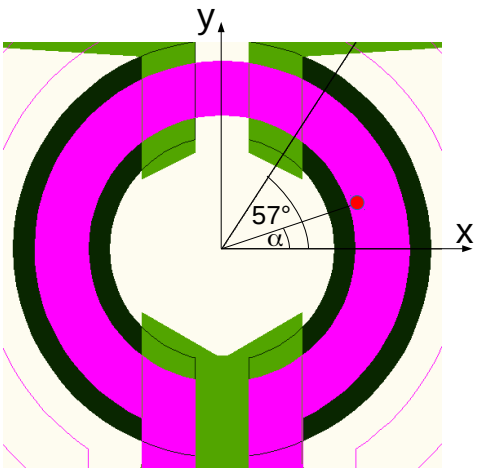

Figure 3.12.: Innermost microring (pink) with the GMR sensor (black) beneath it, the contacts of the GMR sensor (green) and a possible position of a particle (red). The angle of $\sim 57°$ is marked, where the particles will be detected.

integrating over the cosine function:

$$\frac{180}{57\pi}\int_0^{\frac{57\pi}{180}}\cos(\alpha)\mathrm{d}\alpha = \frac{180}{57\pi}\sin\left(\frac{180}{57\pi}\right) = 0.843 \tag{3.20}$$

So the transfer function of the MPs is:

$$T_{particle} = B_{mean}\cdot 0.843 = 230\ \mathrm{nT/particle} \tag{3.21}$$

The average field in x-direction at the GMR sensor generated by the conductor was calculated to:

$$B_{mean} = 565.1\ \mu\mathrm{T} \tag{3.22}$$

Also here the field was averaged over the angle from 0 to 57°.

For the **magnetophoresis-chip** the field was calculated in the same way with the geometry in figure 3.13 and the field of a straight conductor determined in section 3.2.1.

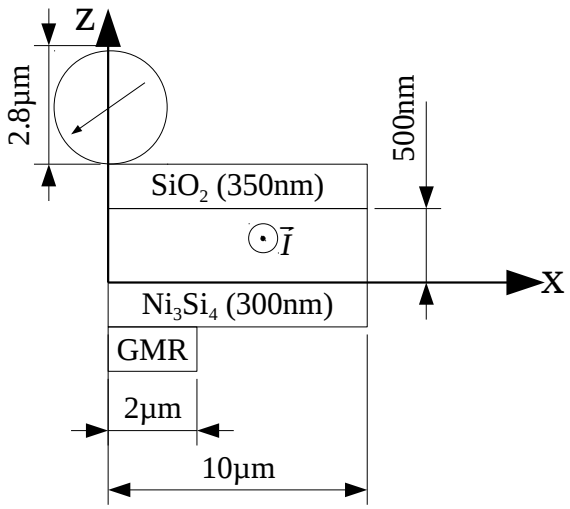

Figure 3.13.: Position of the MP above the conductor and the GMR sensor (for the magnetophoresis-chip).

Figure 3.14a shows the calculated field at the GMR sensor for a current of 10 mA flowing through the conductor. This result was averaged over the area of the GMR sensor to get

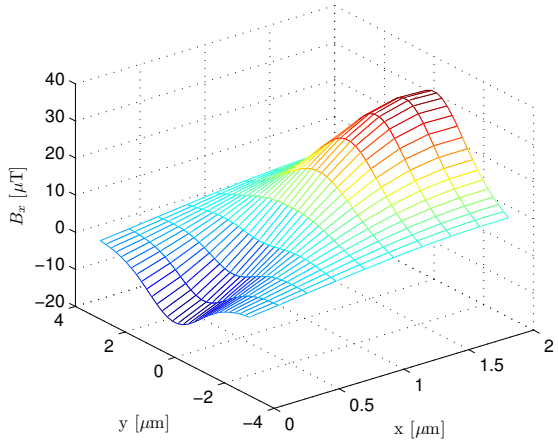

(a) Field in x-direction at the GMR sensor generated by one particle with a current of 10 mA through the rectangular conductor.

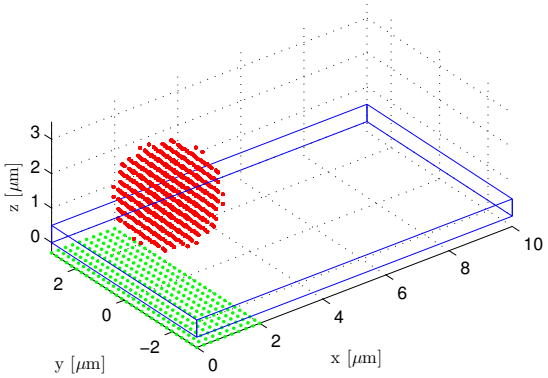

(b) Exact geometry of the simulation with the particle (red), conductor (blue) and GMR sensor (green). The particle and the GMR sensor are drawn by small dots representing the discretisation.

Figure 3.14.: Simulation result and geometry of the magnetophoresis-chip

the mean value:

$$B_{mean} = 9.41\ \mu\mathrm{T} \tag{3.23}$$

The mean magnetic field in x-direction, generated by the conductor, is:

$$B_{conductor} = 556.7\ \mu\mathrm{T} \tag{3.24}$$

3.2.6. The output voltage at the lock-in amplifier

The **microring-chip** consists of four half-ring GMR sensors connected to a Wheatstone bridge, like depicted in figure 3.15. A current of 800μA is applied to the sensor-bridge by a frequency generator. The stray field of a particle results in a resistance change ΔR at one of the GMR sensors, which causes a bridge voltage V_b. By subtracting the voltages at the two lower resistors, V_b can be determined:

$$V_b = V_0 \frac{\Delta R}{4R + 2\Delta R} - \frac{V_0}{2} = V_0 \frac{\Delta R}{4R + 2\Delta R} \tag{3.25}$$

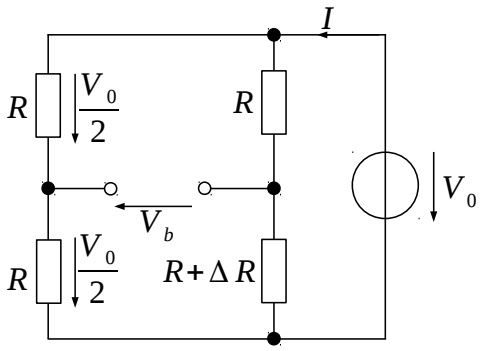

Figure 3.15.: Schematic of the Wheatstone bridge used in the microring-chip

Assuming that $\Delta R << R$ equation (3.25) simplifies to:

$$V_b = V_0 \frac{\Delta R}{4R} = IR\frac{\Delta R}{4R} = I\frac{\Delta R}{4} \tag{3.26}$$

So for $I = 800\mu$A the transfer function of the bridge circuit is:

$$T_{bridge} = 0.0008 \cdot \frac{1}{4} \text{V}/\Omega = 0.2 \text{ mV}/\Omega \tag{3.27}$$

For the measurement two different frequencies have been applied to the GMR sensors and the conductor [13], [14], [15]. The current through the GMR has a frequency of $f_b = 2$kHz. The frequency of the current through the conductor is $f_c = 210$Hz. With the angular frequency ω, this results in a change of the sensor-bridge-voltage of:

$$V_b(t) = \hat{V}_b \sin(\omega_b t) \sin(\omega_c t) \tag{3.28}$$

Using the identity:

$$2 \sin\left(\frac{y+x}{2}\right) \sin\left(\frac{y-x}{2}\right) = \cos x - \cos y \tag{3.29}$$

$V_b(t)$ can be written as:

$$V_b(t) = \frac{\hat{V}_b}{2} \cos\left((\omega_b + \omega_c)\, t\right) - \frac{\hat{V}_b}{2} \cos\left((\omega_b - \omega_c)\, t\right) \tag{3.30}$$

So $V_b(t)$ is a sum of two sine signals at the frequencies $f_1 = f_b + f_c$ and $f_2 = f_b - f_c$. To measure this signal with a lock-in amplifier, the reference frequency has to be set to f_1 or f_2. If the reference frequency is set to f_1 the lock-in amplifier multiplies the signal with a

reference sine signal with the frequency f_1. If the phase shift between the two sine signals is zero the output is [16]:

$$\begin{aligned} V_b(t) \cdot \sqrt{2} \cdot \cos(\omega_1 t) &= \frac{\hat{V}_b}{\sqrt{2}} \cos^2(\omega_1 t) - \frac{\hat{V}_b}{\sqrt{2}} \cos(\omega_1 t) \cos(\omega_2 t) \\ &= \frac{\hat{V}_b}{\sqrt{2}} \cdot \frac{1}{2} (1 + \cos(2\omega_1 t)) - \frac{\hat{V}_b}{\sqrt{2}} \cos(\omega_1 t) \cos(\omega_2 t) \\ &= \frac{\hat{V}_b}{\sqrt{2} \cdot 2} + \frac{\hat{V}_b}{\sqrt{2} \cdot 2} \cdot \cos(2\omega_1 t) - \frac{\hat{V}_b}{\sqrt{2}} \cos(\omega_1 t) \cos(\omega_2 t) \end{aligned} \tag{3.31}$$

After the multiplication the signal is low pass filtered by the lock-in amplifier and only the DC component of the signal remains. So the output of the lock-in amplifier will be $\frac{\hat{V}_b}{\sqrt{2} \cdot 2}$, which is half of the RMS-value.
Thus the transfer function of the lock-in amplifier is:

$$T_{lockin} = \frac{1}{2} \tag{3.32}$$

For measurements with the **magnetophoresis-chip** the GMR sensor R_G was connected to a series resistor R_s and the frequency generator V_0 like depicted in figure 3.16. The lock-in amplifier was connected to the GMR sensor to measure V_G.

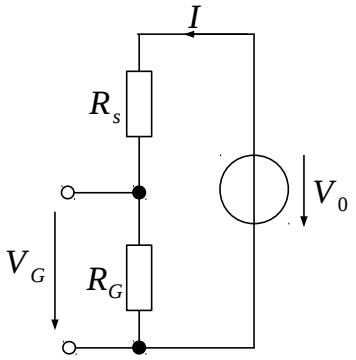

Figure 3.16.: Schematic of the measurement circuit for the magnetophoresis-chip.

The voltage at R_G is:

$$V_G = V_0 \frac{R_G}{R_s + R_G} \tag{3.33}$$

To get the voltage change due to a small resistance change of R_G, the derivative $\frac{\mathrm{d}V_G}{\mathrm{d}R_G}$ was calculated:

$$\frac{\mathrm{d}V_G}{\mathrm{d}R_G} = V_0 \frac{R_G}{(R_s + R_G)^2} \tag{3.34}$$

V_0 was adjusted to conduct a current of $I = 800\ \mu\mathrm{A}$ through the GMR sensor. So V_0 can be expressed as:

$$V_0 = I \cdot (R_s + R_G) \tag{3.35}$$

and $\frac{\mathrm{d}V_G}{\mathrm{d}R_G}$, which is the transfer function of the circuit of the magnetophoresis-chip, can be expressed as:

$$T_{circuit} = \frac{\mathrm{d}V_G}{\mathrm{d}R_G} = I \frac{R_G}{R_s + R_G} = 800\ \mu\mathrm{A} \frac{250\ \Omega}{112.88\ \Omega + 250\ \Omega} = 551\ \mu\mathrm{V}/\Omega \tag{3.36}$$

3.2.7. System transfer function

The transfer function of the **microring-chip** can be written as:

$$\begin{aligned} T &= T_{particle} \cdot S \cdot T_{bridge} \cdot T_{lockin} \\ &= 230\ \mathrm{nT/particle} \cdot 145\ \Omega/\mathrm{T} \cdot 0.2\ \ \mathrm{mV}/\Omega \cdot 1/2 \\ &= 3.33\ \ \mathrm{nV/\,particle} \end{aligned} \tag{3.37}$$

where $S = 145\ \Omega/\mathrm{T}$ is the sensitivity of the GMR sensor.

If the reference-sensors (see section 4.1.1) are not used, there will be an additional voltage at the output due to the magnetic field of the conductor. Because the field of the conductor affects both GMR sensors a factor of 2 needs to be added:

$$\begin{aligned} V_{conductor} &= B_{conductor} \cdot S \cdot T_{bridge} \cdot T_{lockin} \cdot 2 \\ &= 553.7\ \mu\,\mathrm{T} \cdot 145\ \Omega/\mathrm{T} \cdot 0.2\ \ \mathrm{mV}/\Omega \cdot 1/2 \cdot 2 \\ &= 16.1\ \mu\,\mathrm{V} \end{aligned} \tag{3.38}$$

The transfer function of the **magnetophoresis-chip** can be written as:

$$\begin{aligned} T &= T_{particle} \cdot S \cdot T_{circuit} \cdot T_{lockin} \\ &= 9.41\ \mu\text{T/particle} \cdot 1289\ \Omega/\text{T} \cdot 551\ \mu\text{V}/\Omega \cdot 1/2 \\ &= 3.34\ \mu\,\text{V/ particle} \end{aligned} \tag{3.39}$$

where $S = 1289\Omega/\text{T}$ is the sensitivity of the GMR sensor.

The additional voltage at the output due to the magnetic field of the conductor is:

$$\begin{aligned} V_{conductor} &= B_{conductor} \cdot S \cdot T_{bridge} \cdot T_{lockin} \cdot 2 \\ &= 556.7\ \mu\,\text{T} \cdot 1289\ \Omega/\text{T} \cdot 551\ \mu\text{V}/\Omega \cdot 1/2 \\ &= 197.8\ \mu\,\text{V} \end{aligned} \tag{3.40}$$

3.3. Design Requirements and Consideration

As already stated in the previous section, the MPs will be attracted to the maximum of the magnetic field above the conductor and their position can thus be determined from the magnetic field of the conductor in figure 3.3 and 3.8. For a straight wire the particles will be attracted to the edges of the conductor and for a microring, they will move to the inner edge of the conductor.

In figure 3.17 the magnetic field at the GMR sensor for different positions of an MP above a microring conductor is shown. Depending on the position, the MPs are magnetised in different directions and will produce a different stray field at the GMR sensor. The field decreases very fast with the distance to the MP. To achieve maximum output for single particle detection, it would be best to produce a small GMR sensor at the position, where the maximum of the field is expected. This was done for the magnetophoresis-chip, where single particles shall be detected, when they arrive at the conductor. In figure 3.18 the field of a particle above a straight conductor is depicted. Because the particle is attracted to the edge of the conductor also the field of the particle shows a high peak at the edge. Thus the GMR sensor for the magnetophoresis-chip was placed at the edge with a width of 2 μm to cover the peak of the magnetic field.

If more particles are present, they will be distributed all over the conductor. A small GMR sensor would only be sensitive to the MPs in close proximity and the other MPs would have no effect on the output. Therefore it is necessary to have a GMR sensor, which is about the size of the conductor, to measure the concentration of MPs in a solution. This was done in the microring-chip, which was designed to detect larger quantities of particles.

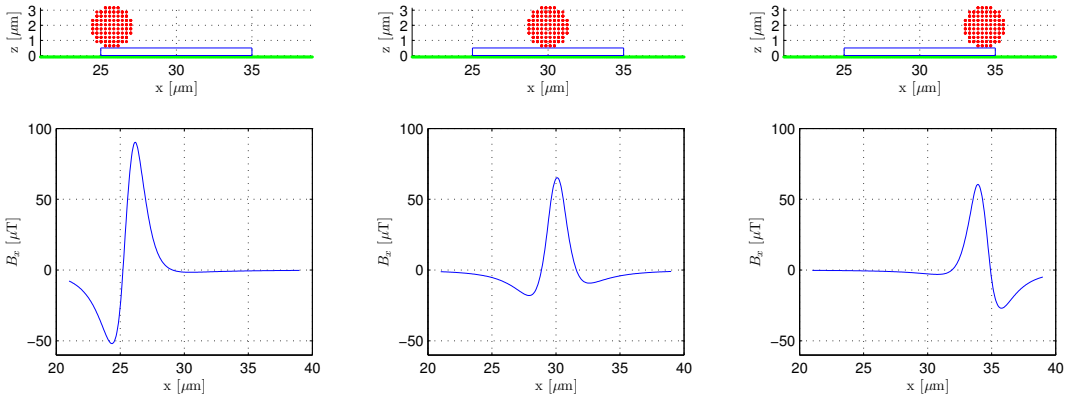

Figure 3.17.: Magnetic field in x-direction from a magnetised particle at the GMR sensor beneath the particle ($d = 2.8$ μm, $\chi = 1.0$) for different positions of the particle and a current of 10 mA flowing through the conductor. On the top the geometry of the calculation is depicted with the particle (red), the conductor (blue), the GMR sensor (green) and a 100 nm passivation layer between the conductor and the GMR sensor.

The distance that separates the GMR sensor from the MPs is an important parameter to consider with respect to the detection of the magnetic stray fields and the sensitivity. The separation is due to the conductor, a passivation layer 1, insulating the GMR sensor from the conducting ring structure and an optional passivation layer 2, protecting the ring structure from corrosive and conducting sample solutions. From experimental results and taking into account heating and electromigration limits, a thickness of 500 nm is reasonable for the conducting ring element [17]. Hence, flexibility to control the distance between the GMR sensor and MPs is available from the thickness of the passivation layers.

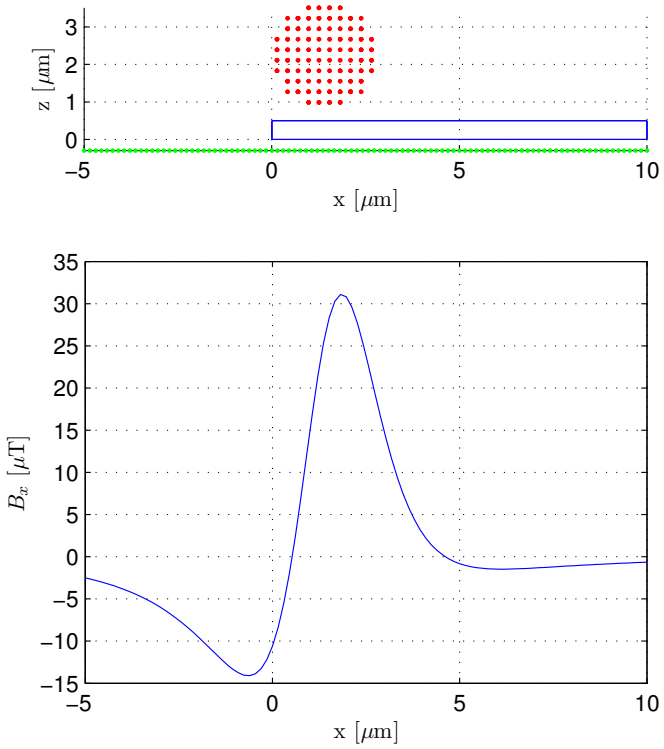

Figure 3.18.: Magnetic field in x-direction from a magnetised particle at the z-position of the GMR sensor beneath the particle ($d = 2.8$ μm, $\chi = 1.0$) for a current of 10 mA flowing through the conductor. On the top the geometry of the calculation is depicted with the particle (red), the conductor (blue), the GMR sensor (green) and two 300 nm passivation layers between the particle, the conductor and the GMR sensor.

4. Chip Development and Characterisation

4.1. Chip Design

The principle design of both chips consists of a microfluidic channel with inlets and outlets, placed on top of a layer with current carrying microstructures to establish the needed magnetic field gradient for the manipulation of the MPs. Beneath the conductors are the GMR sensors, which are separated by an insulation layer.

4.1.1. Design of the Microring-chip

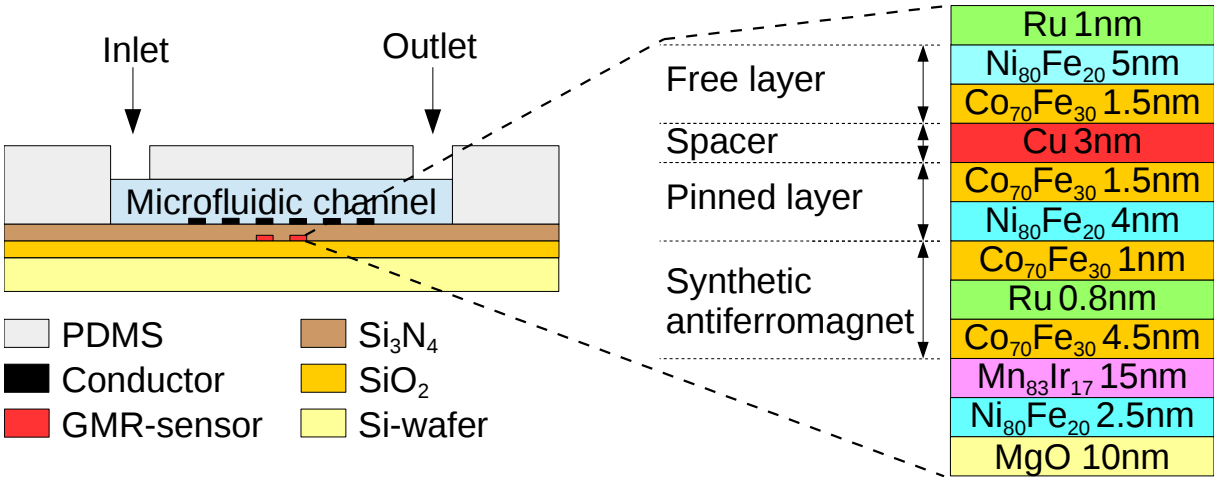

Figure 4.1.: Layers of the microring-chip and the GMR sensor.

The developed chip in figure 4.1 consists of several layers produced on an Si-wafer as the substrate. The Si-wafer is equipped with a 50 μm SiO_2 insulation layer. On top of the SiO_2 layer the GMR-stack depicted on the right side of figure 4.1 was deposited and covered with a 100 nm Si_3Ni_4 passivation layer. 500 nm thick round gold conductors are

directly above the GMR sensors. The 110 μm thick microfluidic channel was constructed by placing a PDMS structure on top of the chip.

The GMR-stack in figure 4.1 consists in principle of a synthetic antiferromagnet, a pinned layer, a spacer and a free layer like described in section 2.3. The synthetic antiferromagnet (SAF) consisting of $Co_{70}Fe_{30}$/Ru/$Co_{70}Fe_{30}$ was exchange coupled with an $Mn_{83}Ir_{17}$ layer. A 0.8 nm thick Ru layer provides strong antiparallel coupling between the CoFe layers.

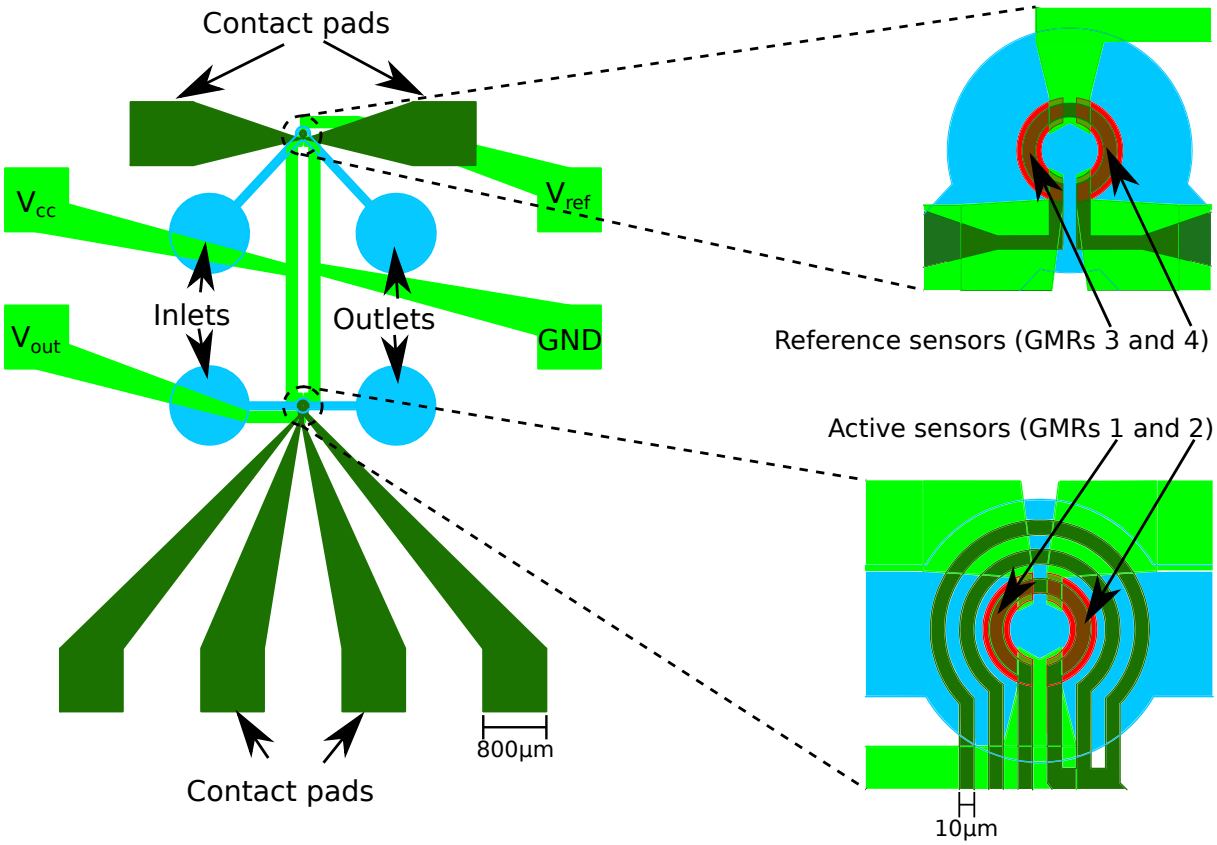

Figure 4.2.: Schematic of the microring-chip with the current carrying microstructure, GMR sensors, GMR-contact-leads and microfluidic channels with inlets and outlets, as used for the masks for fabrication.

In this device half-ring GMR sensors are used for MP detection. The design of the chip is depicted in figure 4.2. Three microrings with a width of 10 μm are used to attract particles to the active GMR sensors, by turning them on sequentially from the outermost to the innermost. The two active sensors are connected to two reference sensors in a Wheatstone bridge architecture (figure 4.3) to compensate for thermal and electrical drift and bias signals. All four GMR sensors and the conductors above them are designed with exactly the same dimensions. In this way, GMRs 1 and 2 have the same lower resistance and GMRs 2 and 4 have the same high resistance, when no MPs are present, resulting

in a zero differential output ($V_{out} - V_{ref}$). When MPs are present, their stray magnetic fields affect only GMRs 1 and 2, changing their resistance values in opposite directions. This produces a measurable differential voltage output.

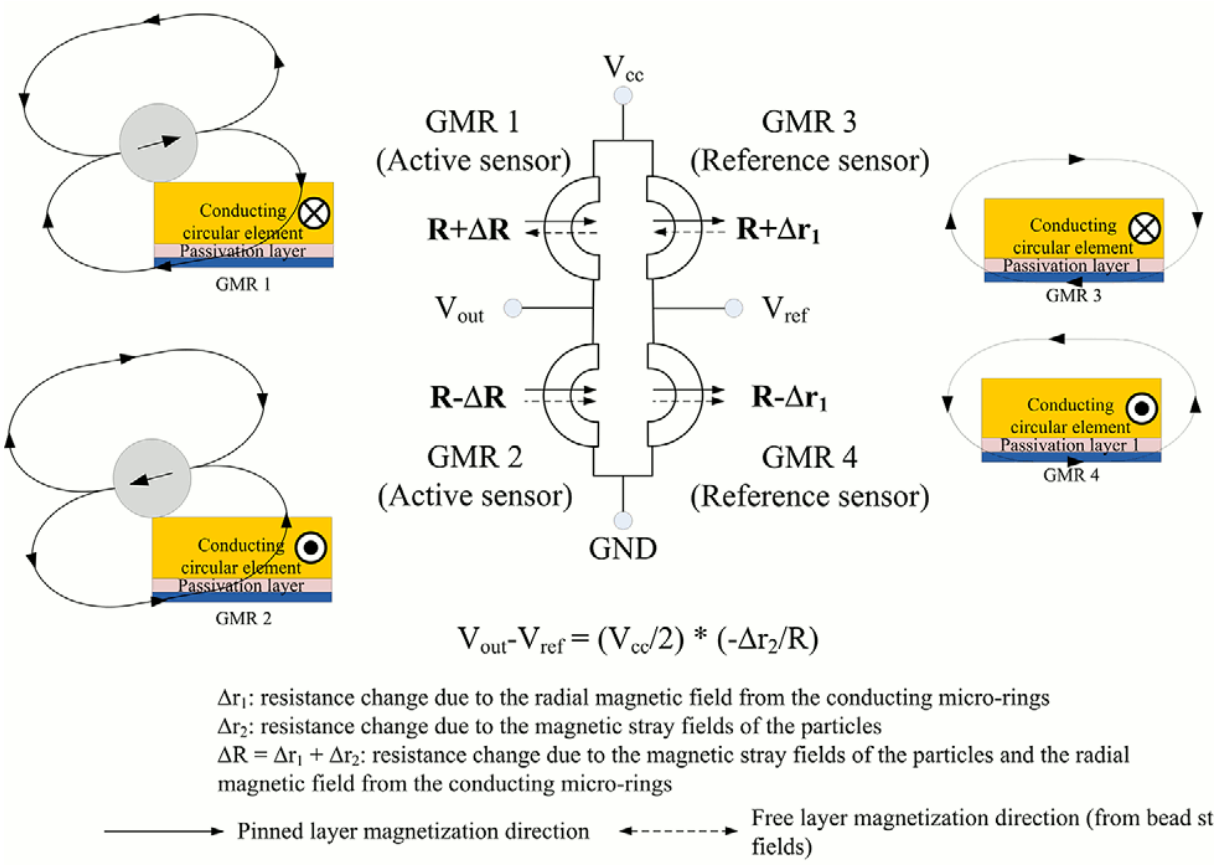

Figure 4.3.: Wheatstone bridge connection of the GMR sensors.

4.1.2. Design of the Magnetophoresis-chip

The developed chip in figure 4.4 consists of several layers produced on an Si-wafer equipped with a 50 μm SiO_2 insulation layer. On top of the SiO_2 layer the GMR-stack depicted on the right side of figure 4.4 was deposited and covered with a 300 nm Si_3Ni_4 passivation layer. 500 nm thick aluminium conductors are directly above the GMR sensors and covered with a 350 nm SiO_2 passivation layer. The 110 μm thick microfluidic channel was constructed by placing a PDMS structure on top of the chip.

The GMR-stack in figure 4.4 consists in principle of a pinned layer, a spacer and a free layer like described in section 2.3. The lowest CoFe layer was exchange coupled with a

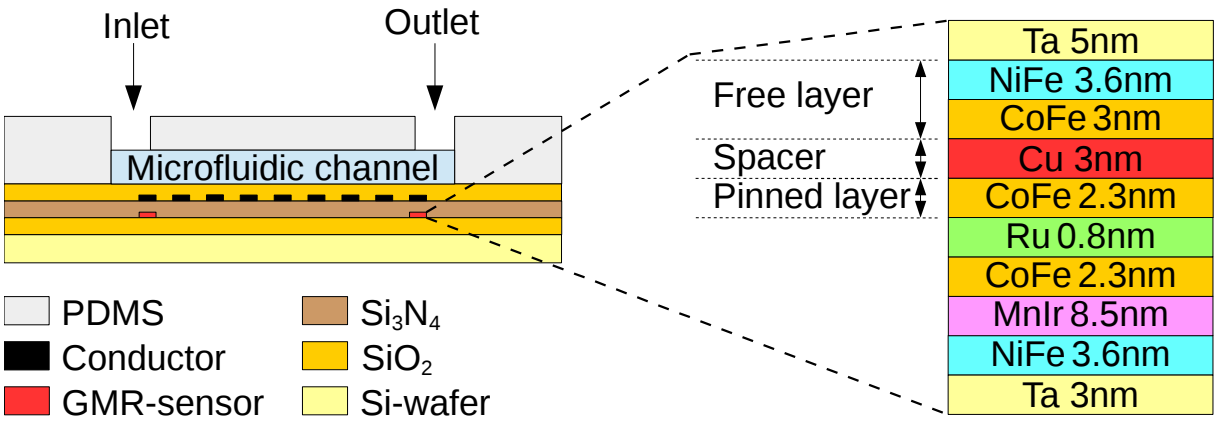

Figure 4.4.: Layers of the magnetophoresis-chip and the GMR sensor.

MnIr layer. A 0.8 nm thick Ru layer provides strong antiparallel coupling between the lowest CoFe layer and the pinned layer.

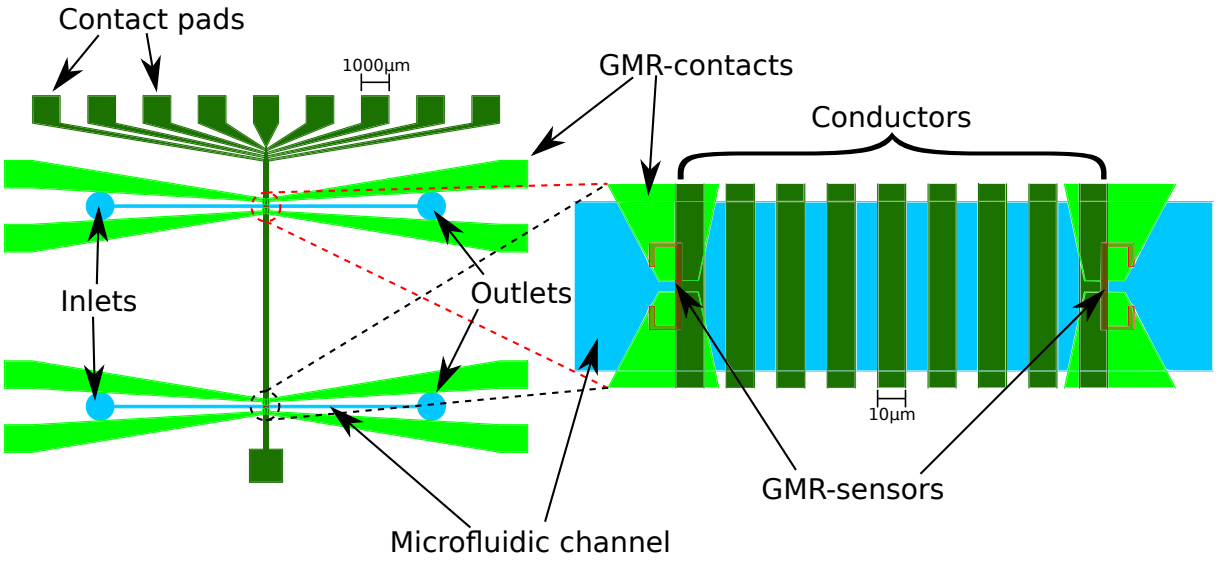

Figure 4.5.: Schematic of the magnetophoresis-chip with the current carrying microstructure, GMR sensors, GMR-contact-leads and microfluidic channels with inlets and outlets, as used for the masks for fabrication.

The design of the magnetophoresis-chip is depicted in figure 4.5. 9 straight conductors with a width of 10 μm are used to move MPs from one side to the other by applying currents sequentially. At the first and the last conductor GMR sensors with an active area of 2 μm×6μm were fabricated. The structure with the microfluidic channel and the GMR sensors was fabricated two times to have more opportunities for measurements. Each of the four GMR sensors can be contacted individually.

4.2. Fabrication

4.2.1. Fabrication of the microring-chip

The microring-chip was fabricated at the Austrian Institute of Technology (AIT) in the following steps:

1. The "bottom" spin valve structure: MgO 10/$Ni_{80}Fe_{20}$ 2.5/$Mn_{83}Ir_{17}$ 15/$Co_{70}Fe_{30}$ 4.5/Ru 0.8/$Co_{70}Fe_{30}$ 1/$Ni_{80}Fe_{20}$ 4/$Co_{70}Fe_{30}$ 1.5/Cu 3/$Co_{70}Fe_{30}$ 1.5/$Ni_{80}Fe_{20}$ 5/Ru 1 (thicknesses in nm) was deposited using a Leybold Univex 450C magnetron sputtering system on an oxide-coated Silicon wafer.

2. A transverse magnetisation direction was induced in the pinned layer during annealing at a temperature of 250°C under an applied magnetic field of 600 Oe. The layers were then cooled at room temperature in a magnetic field.

3. After deposition, spin valve elements were patterned by electron beam lithography with an electron dose of 140 - 200 $\mu C/cm^2$. This was followed by ion beam milling with Ar gas, at an angle of 45°, beam current of 45 mA, beam and accelerator voltage of 500 V and a process pressure of 10^{-4} mbar.

4. Au was sputtered as conducting leads to the GMR sensing element.

5. The sensing elements were covered with a 100 nm Si_3N_4 passivation layer for covering the spin valve GMR elements and lead conductors except parts of the connection/bonding pads.

6. The conducting microring structure was fabricated of 500 nm thick Au with a 10 nm thick Ti adhesion layer on top of the sensor using photolithography and lift-off techniques.

4.2.2. Fabrication of the magnetophoresis-chip

The magnetophoresis-chip was fabricated at the Institute for Systems Engineering and Computers (INESC) in Portugal with the following steps:

1. The "bottom" spin valve structure: Ta 3/NiFe 3.6/MnIr 8.5/CoFe 2.3/Ru 0.8/CoFe 2.3/Cu 3/CoFe 3/NiFe 3.6/Ta 5 (thicknesses in nm) was sputtered on an oxide-coated Silicon wafer.

2. A photoresist was dispensed, exposed and developed.

3. The sensors were etched by Ion beam Milling.
4. The photoresist was stripped in a wet bench with ultrasound.
5. The resist for the contacts was dispensed, exposed and developed.
6. 300 nm of aluminium were deposited for the sensor contacts.
7. Aluminium Lift-Off
8. A 300 nm Si_3N_4 passivation layer 1 was deposited.
9. The photoresist was dispensed, exposed and developed.
10. Openings for the contact pads were etched in the passivation layer with reactive ion etching.
11. The resist was stripped.
12. The photoresist was dispensed, exposed and developed.
13. 500 nm of gold with a 5 nm adhesion layer of titanium was deposited.
14. Gold lift-Off
15. A 350 nm SiO_2 passivation layer was deposited.
16. The photoresist was dispensed, exposed and developed.
17. Openings for the contact pads were etched in the passivation layer 2 with reactive ion etching.
18. The resist was stripped.
19. Anealing was performed for 15 min at 250°C. The wafer was cooled down to 80°C in vacuum, while applying a magnetic field of 1 T to magnetise the pinned layer.

4.2.3. Fabrication of the microfluidic channel

First a mould was created with Ordyl SY300. Ordyl is a negative-type dry-film photoresist, manufactured by Elga Europe. It is available in thicknesses from 15 μm to 55 μm. For the mould two layers of 55 μm (Ordyl SY355) were utilised.

Processing Ordyl consists of three major steps (see Figure 4.6):

(a) Lamination of the dry film to the substrate

(b) UV exposure with a mask to pattern the desired structure

(c) Development

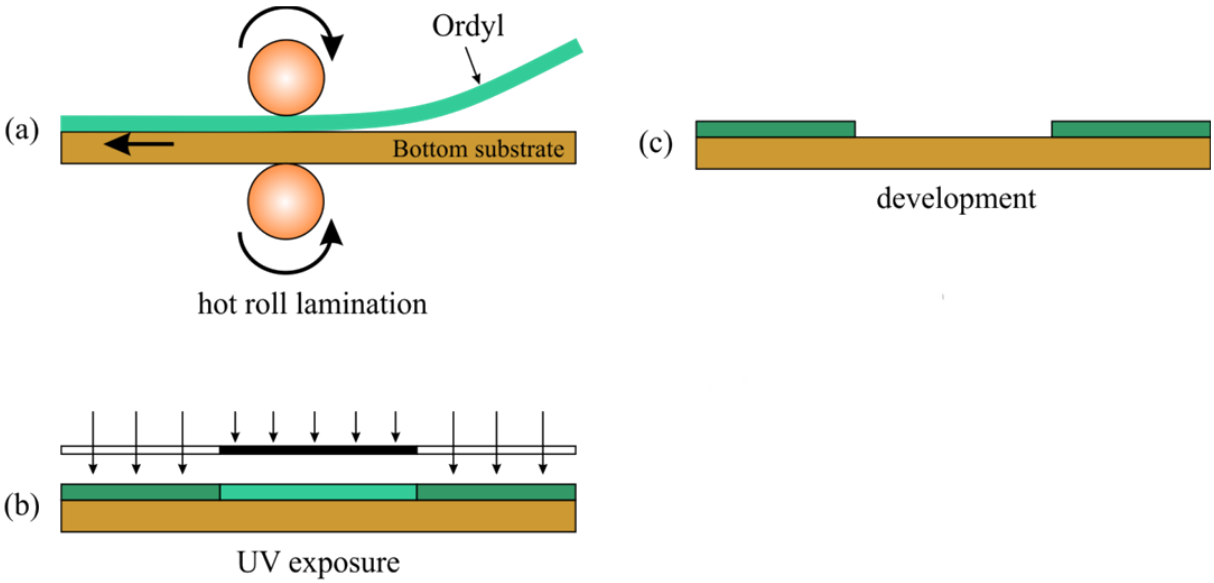

Figure 4.6.: Ordyl processing steps

The channel was made with Polydimethylsiloxane (PDMS), a soft polymer that is widely used to make cheap, disposable microfluidic devices [18]. The PDMS we used is Sylgard 184 from Dow Corning, a two-part heat curable system that is mixed 10:1 (w/w) with the included curing agent. The creation of the channel with the previously manufactured mould and the PDMS included the following steps:

1. The PDMS was mixed in a petri dish.
2. Bubbles, which were introduced during mixing, were degassed in a centrifuge.
3. The PDMS was slowly poured on the photolithographic mould. If bubbles formed near the channel, they were removed with tweezers.
4. The PDMS was cured in an oven at 80°C for 1 hour.
5. The channel was cut out with a sharp razor blade.
6. The cut-out PDMS was peeled off the substrate and placed in a new petri dish, to keep it as clean as possible.

7. A sharpened hollow wire was used to make inlet and outlet holes.

Before each measurement the channel was cleaned with aceton and isopropanol and placed on the chip with tweezers.

4.3. Characterisation of the GMR sensors

Spin-valve GMR sensors are mostly sensitive to magnetic fields parallel to the magnetisation of the pinned layer. The resistance change due to magnetic fields in other directions can be neglected. Both GMR sensors were placed in a uniform magnetic field in sensitive direction produced by a Helmholtz coil. The field strength was varied and the resistance was measured to obtain the diagrams in figure 4.7. The field strength was varied in both directions to determine the hysteresis of the sensors. The sensitivity for small signals was determined from the gradient in the linear region around zero magnetic field. The obtained sensitivity is 145 Ω/T for the microring-chip and 1289 Ω/T for the magnetophoresis-chip.

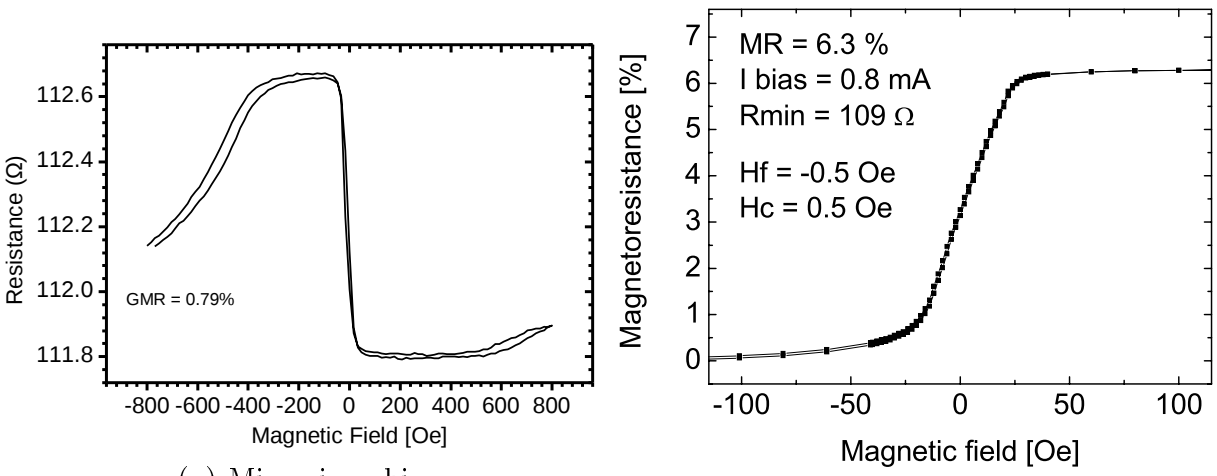

(a) Microring-chip

(b) Magnetophoresis-chip

Figure 4.7.: Characterisation curves of the GMR-sesnors.

4.4. Experimental Set-up

The measurement setup to manipulate and detect particles is depicted in figure 4.8 To actuate the currents on the conductor a series of manual switches was used. LEDs were

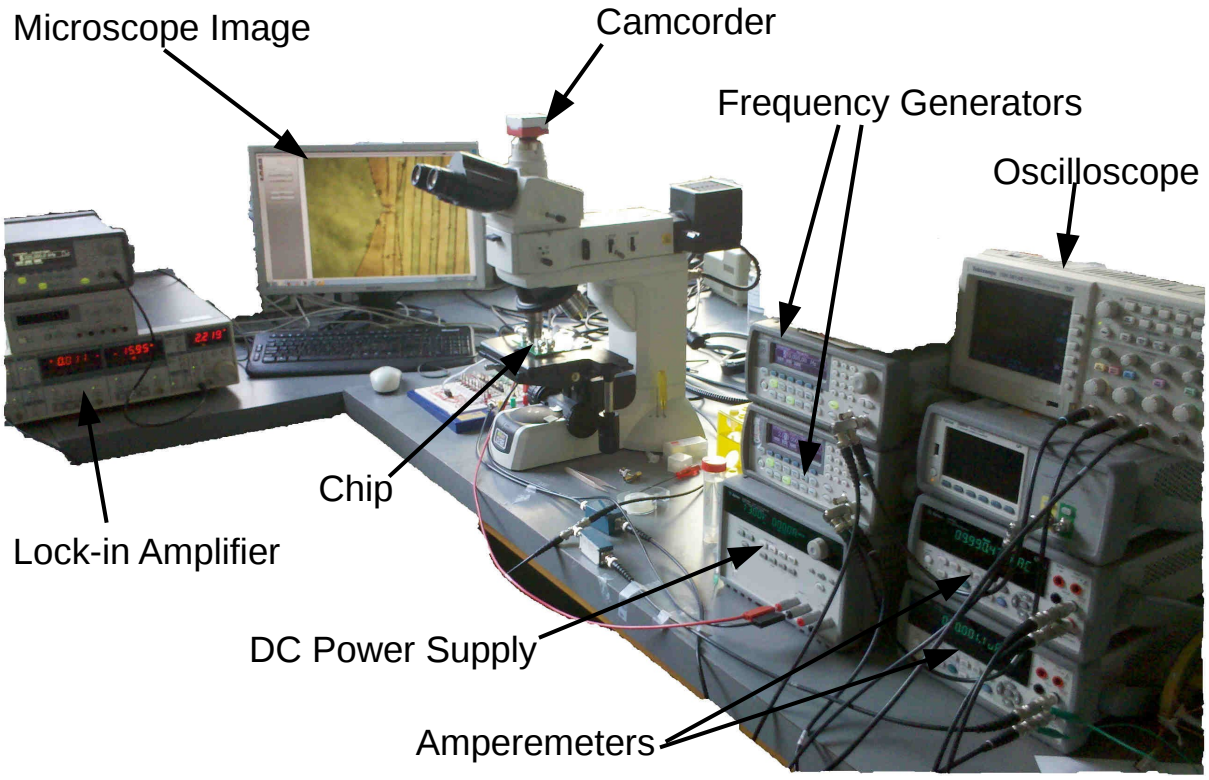

Figure 4.8.: Measurement setup.

used to visualise when a conductor was turned on. The DC-power-supply was used to attract the MPs to the GMR sensor. A mixing technique was used to measure the stray field of the MPs. Two frequency generators were used to apply two different frequencies to the GMR sensor and the conductor above the GMR sensor. The voltage change across the GMR sensor was measured with the Lock-in amplifier at the sum of the two frequencies to avoid crosstalk and reduce noise. The output of the Lock-in amplifier was recorded by a PC, which was connected to the GPIB-interface. To monitor the currents through the GMR sensor and the conductors two amperemeters were used. The chips were placed on a microscope. A camera was mounted on the microscope and connected to a PC via USB to capture the position of the MPs.

A close up on the two chips beneath the microscope is depicted in figure 4.9. The microring-chip and the magnetophoresis-chip are mounted with a double-faced adhesive tape on a DIP package and a PCB. The contact pads are connected to the DIP package and the PCB via wire bonding using gold wires. All connections to the GMR sensors and the conductors directly above the GMR sensors have been made with coaxial cables to minimise noise.

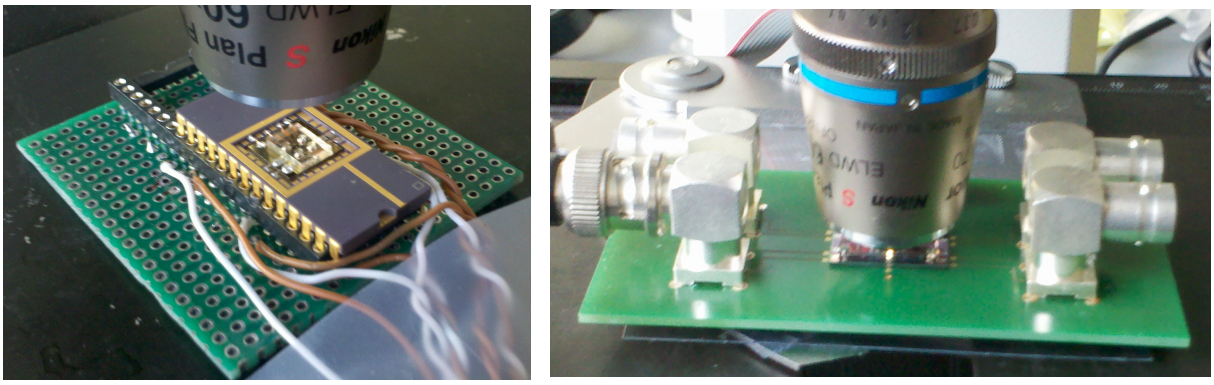

(a) Microring-chip (b) Magnetophoresis-chip

Figure 4.9.: Mounting of the chips on the DIP package and the PCB.

4.5. Measurement utilities

For the Measurements Dynabeads 270 and Dynabeads MyOne were used. For the magnetic properties see table 4.1. These are hydrophilic Dynabeads with carboxylic acid groups. These surface groups allow covalent amide bond formation to proteins/peptides via primary amino- or sulphydryl groups. The Dynabeads are supplied in an aqueous suspension with a concentration of $2 \cdot 10^9$ particles/ml for Dynabeads 270 and $7 - 12 \cdot 10^9$ particles/ml. To achieve lower concentrations the particle suspension was mixed with DI-water before each measurement.

To administer the particle solutions to the microfluidic channel a 1 mL syringe, a 0.8 mm cannula and a piece of rubber tube were combined (see Figure 4.10). For each experiment a small amount of particle solution was drawn into the syringe, the rubber tube end was placed on the inlet of the microfluidic channel and the particle solution was brought into the channel by carefully administering pressure on the syringe. The same tool was used to clean the channel after each experiment by flushing it with DI-water.

Dynabeads product	**Diam. (μm)**	**Magnetic Susceptibility**		**Saturation Magnetisation**		**Iron content**
		m^3/kg (mass)	**Magnetisation (volume)**	**Am^2/kg (mass)**	**kA/m (volume)**	
MyOne Dynabeads	1.0	$8 \cdot 10^{-4}$	1.4	24	43	26
M-270 Dynabeads	2.8	$6 \cdot 10^{-4}$	1.0	13	20	14

Table 4.1.: Magnetic properties of Dynabeads (typical values)

Figure 4.10.: A 1 mL syringe, a 0.8 mm cannula and a piece of rubber tube (top) that were combined (bottom) to create a tool for administering the particle solutions to the microfluidic channel.

5. Results and Discussion

Several measurements have been performed with both chips, detecting Dynabeads 270 and MyOne. Calculations have been performed, as presented in section 3.2 for comparison.

5.1. Measurement with the microring-chip and Dynabeads 270

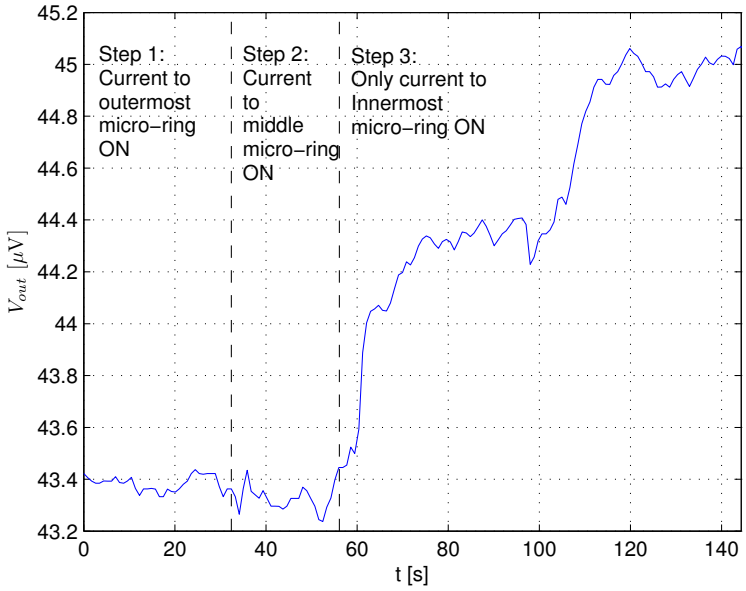

Figure 5.1.: Output at the lock-in amplifier over the time t. The microrings were switched on sequentially from the outermost to the innermost to bring the particles to the center. When the particles arrived at the center the output voltage increased.

For the measurement 5 μl of "Dynabeads M-270 Carboxylic Acid" were suspended in 1ml of deionised water. The particles have a diameter of $d = 2.8$ μm and a susceptibility of $\chi = 1.0$.

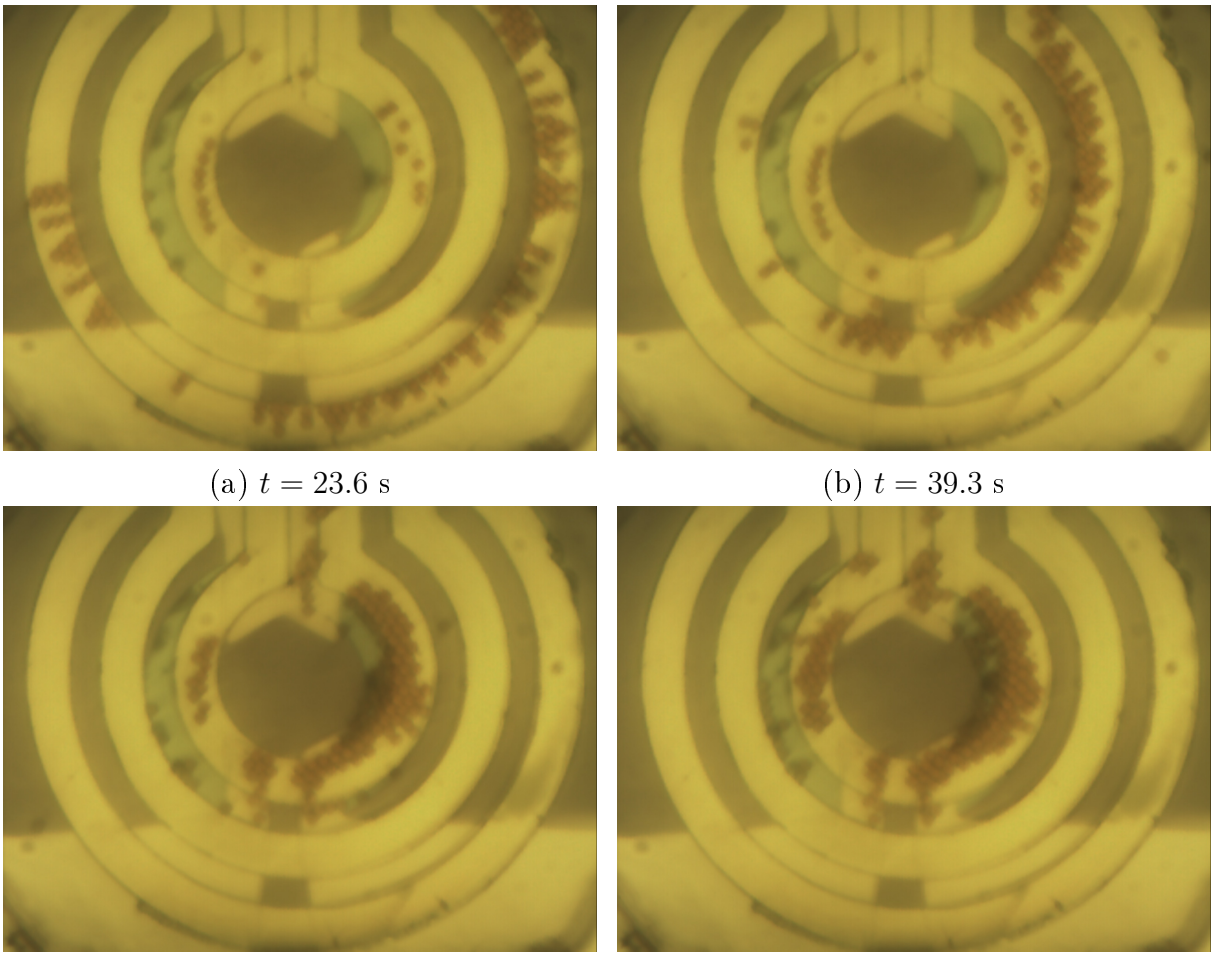

(a) $t = 23.6$ s (b) $t = 39.3$ s

(c) $t = 78.7$ s (d) $t = 135.6$ s

Figure 5.2.: Sensor with particles at different timepoints.

For measuring the stray field of the particles a current of 20 mA with a frequency of 210 Hz was applied to the innermost microring and a current of 800 μA with a frequency of 2 kHz was applied to the GMR sensor beneath the microring. The reference sensors have not been used, since they showed low resistance to the GMR-contacts, probably due to a failure in the fabrication process.

With the lock-in amplifier the bridge-voltage of the GMR sensors was measured at a frequency of 2210 Hz. The output of the lock-in amplifier is depicted in figure 5.1. The currents through the innermost microring and the GMR sensors have been on for the whole measurement. During step 1 particles were attracted to the outermost microring (figure 5.2a) by applying a DC current of 20 mA. At step 2 the outermost microring was switched off and the same current was applied to the middle microring (figure 5.2b). At step 3 the middle microring was turned off and the particles were attracted to the innermost microring (figure 5.2c). Now the voltage increased because the particles were above the GMR sensors. After some time more particles were attracted to the innermost microring (figure 5.2d) resulting in a further increase of the voltage.

At step 3 the voltage first increased by 0.9 μV and the amount of particles above the GMR sensors increased from 18 (figure 5.2a) to 93 (figure 5.2c). This corresponds to a voltage change per particle of 12 nV.

When the output voltage further increased an amount of 121 particles (figure 5.2d) was above the sensor and the voltage increased by 1.6 μV compared to the beginning. This corresponds to a voltage change per particle of 15.4 nV. The different voltage change per particle can be explained by the fact, that the voltage change also depends on the position of the particles. Thus the concentration can not be determined exactly from the sensor output.[15]

Comparison with simulation

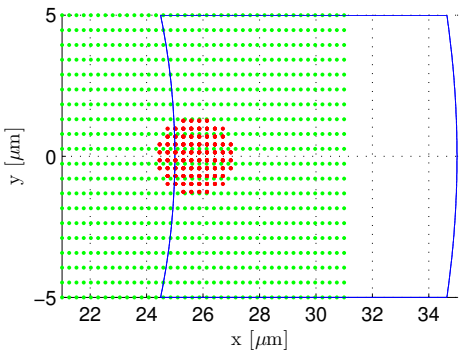

(a) Top view

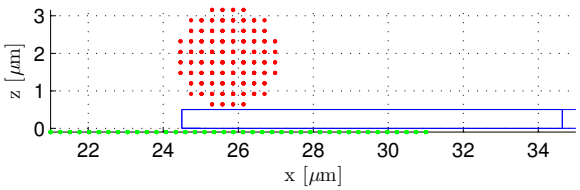

(b) Side view

Figure 5.3.: Position of the particle (red), conductor (blue) and GMR sensor (green) at the simulation with Matlab. The GMR sensor and the particles are drawn by small dots showing the discretisation.

A simulation was performed with Matlab to calculate the output voltage at the GMR sensor. The geometry of the model is shown in figure 5.3, where the particle is at its most probable position determined in section 3.2.4. For the field from the conductor an output voltage of 16.4 μV was calculated and a voltage of 43.4 μV was measured. For the field of one particle a voltage change of 4.32 nV was calculated and a voltage change of 12-15.4 nV was measured.

There are several reasons for the difference between measurement and calculation. The chip was not produced perfectly, which is apparent in figure 5.2, where the GMR sensor is obviously shifted to the conductors unlike the design in figure 4.5. The calculations were based on the design of the chip, which could lead to the difference. Several assumptions

were made to simplify the calculation. Additionally, not all of the particles have exactly the size and susceptibility specified in the datasheet, and there is always some noise, which can influence the measurement.

5.2. Measurement with the magnetophoresis-chip and Dynabeads 270

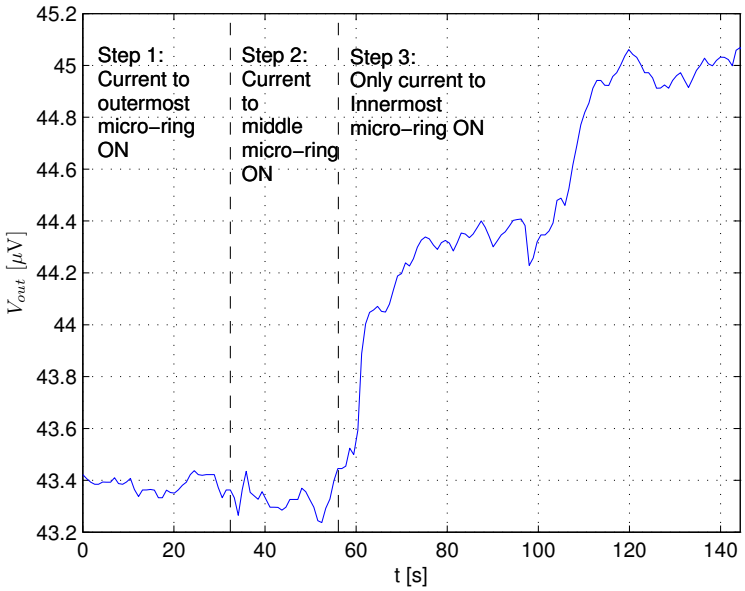

Figure 5.4.: Output at the lock-in amplifier over the time t. The output changes with the amount of particles above the sensor.

For the measurement 10 μl of "Dynabeads M-270 Carboxylic Acid" were suspended in 1 ml of deionised water. The particles have a diameter of $d = 2.8$ μm and a susceptibility of $\chi = 1.0$.

For measuring the stray field of the particles a current of 10 mA with a frequency of 210 Hz was applied to the conductor and a current of 800 μA with a frequency of 1 kHz was applied to the GMR sensor beneath the conductor. With the lock-in amplifier the voltage at the GMR sensor was measured at a frequency of 1210 Hz.

The output of the lock-in amplifier is depicted in figure 5.4. The dashed vertical lines indicate the timepoints, when the pictures in figure 5.5 were made. From $t = 50$ s to $t = 170$ s a constant amount of particles was above the sensor (figure 5.5a). Then the

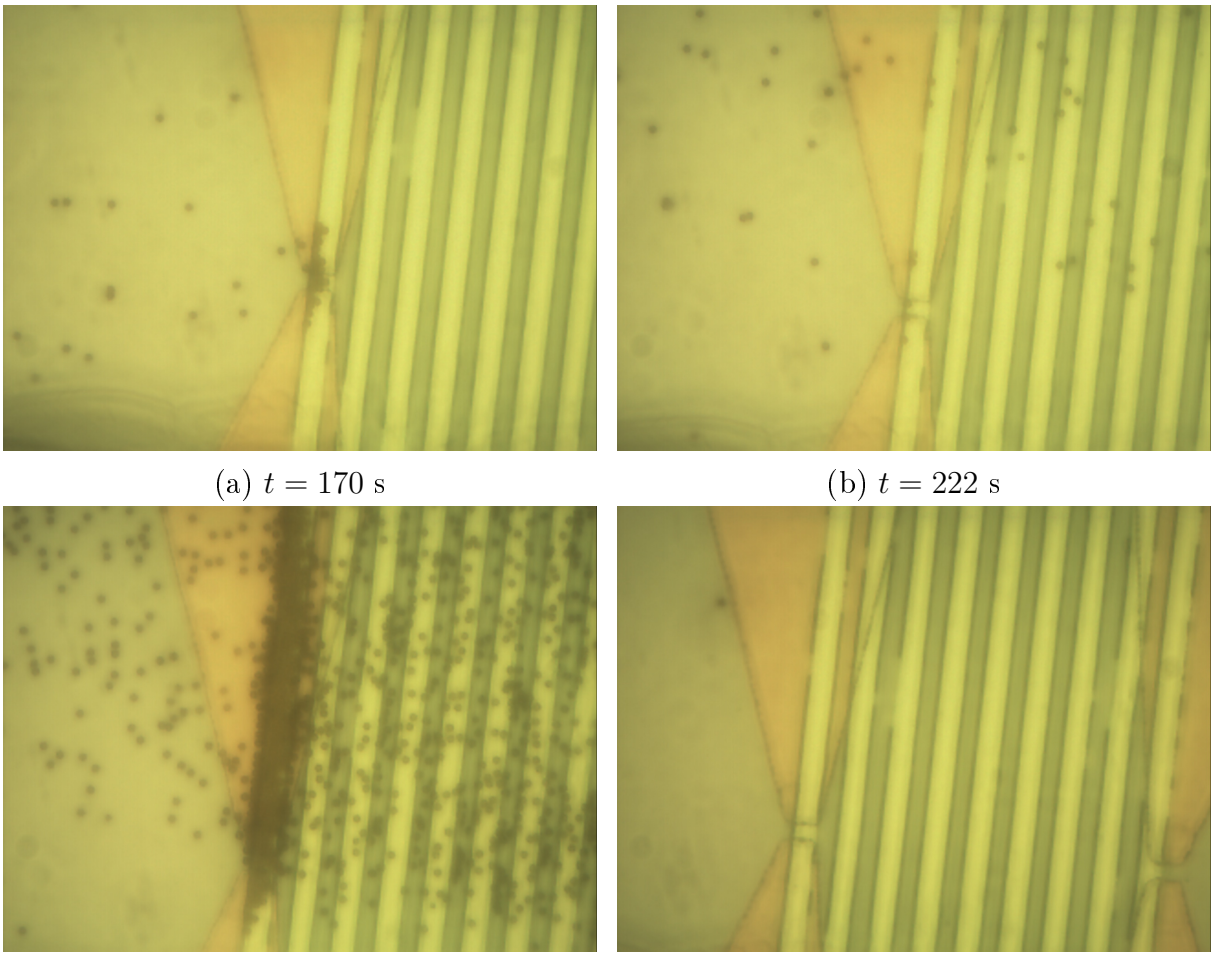

(a) $t = 170$ s (b) $t = 222$ s

(c) $t = 353$ s (d) $t = 583$ s

Figure 5.5.: Sensor with particles at different timepoints.

particles were washed away and the voltage dropped to 155 μV. Again particles started to move towards the GMR sensor and the voltage increased to 165 μV (see figure 5.5b and 5.5c for the amount of particles). The particles were washed away again and the voltage dropped again to 155 μV (figure 5.5d). At points, where the voltage dropped below 140 μV, the current through the conductor was turned off. [15]

Comparison of measurement and simulation

A simulation was performed with Matlab to calculate the output voltage at the GMR sensor. The geometry of the model is shown in figure 5.6. For the field from the conductor an output voltage of 197.8 μV was calculated and a voltage of 155.5 μV was measured.

Since the sensor is about the same size as the particles, the output voltage due to a particle depends very much on the particle position. So the output voltage change was calculated for all particles close to the GMR sensor. The position of the particles for the geometry of

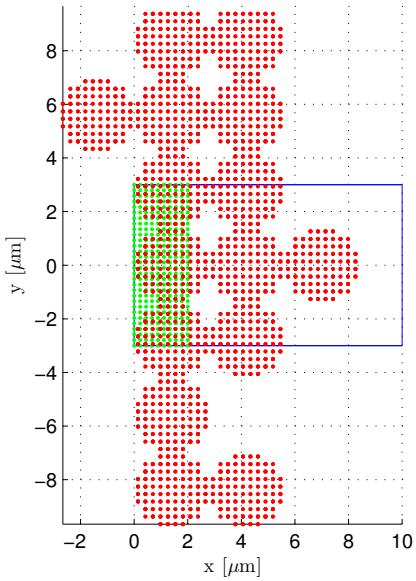

(a) Top view

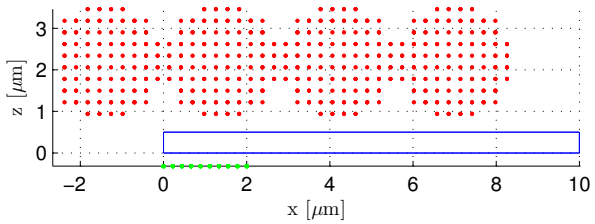

(b) Side view

Figure 5.6.: Position of the particle (red), conductor (blue) and GMR sensor (green) at the simulation with Matlab. The GMR sensor and the particles are drawn by small dots showing the discretiazation.

the simulation in figure 5.6 has been determined approximately from figure 5.5a. For the field of these particles a voltage change of 6.68 μV was calculated and a voltage change of 5 μV was measured.

The difference between the measurement and the simulation could be due to a shift of the position of the GMR sensor. Since the GMR sensor is only 2 μm wide a small shift of the GMR sensor would already cause a big difference. Apart from that the arguments for the microring-chip also apply here.

5.3. Measurement with the magnetophoresis-chip and Dynabeads MyOne (reduced sensitivity)

For the measurement 20 μl of "Dynabeads MyOne" were suspended in 1 ml of deionised water. The particles have a diameter of $d = 1$ μm and a susceptibility of $\chi = 1.4$.

For measuring the stray field of the particles a current of 10 mA with a frequency of 210 Hz was applied to the conductor and a current of 800 μA with a frequency of 2010 Hz was applied to the GMR sensor beneath the conductor. With a lock-in amplifier the voltage at the GMR sensor was measured at a frequency of 2220 Hz.

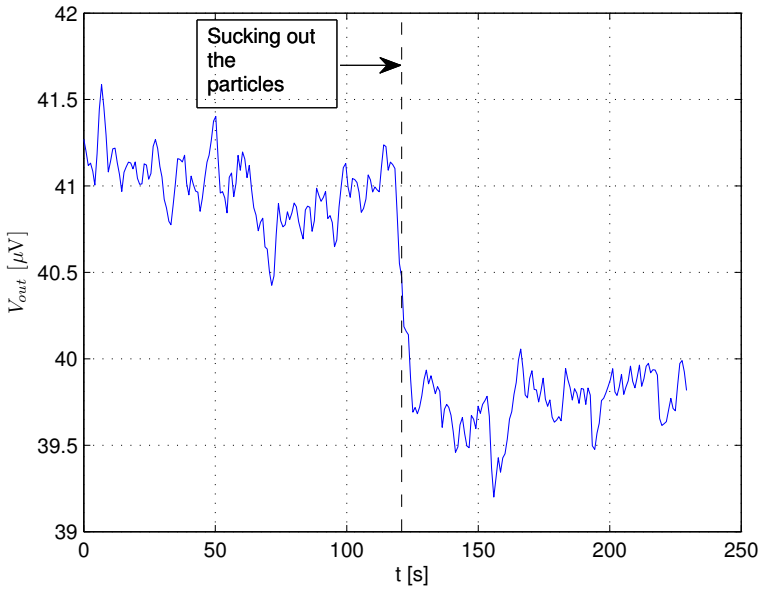

Figure 5.7.: Output at the lock-in amplifier over the time t. The output changes with the amount of particles above the sensor. The output decreases after sucking out the particles.

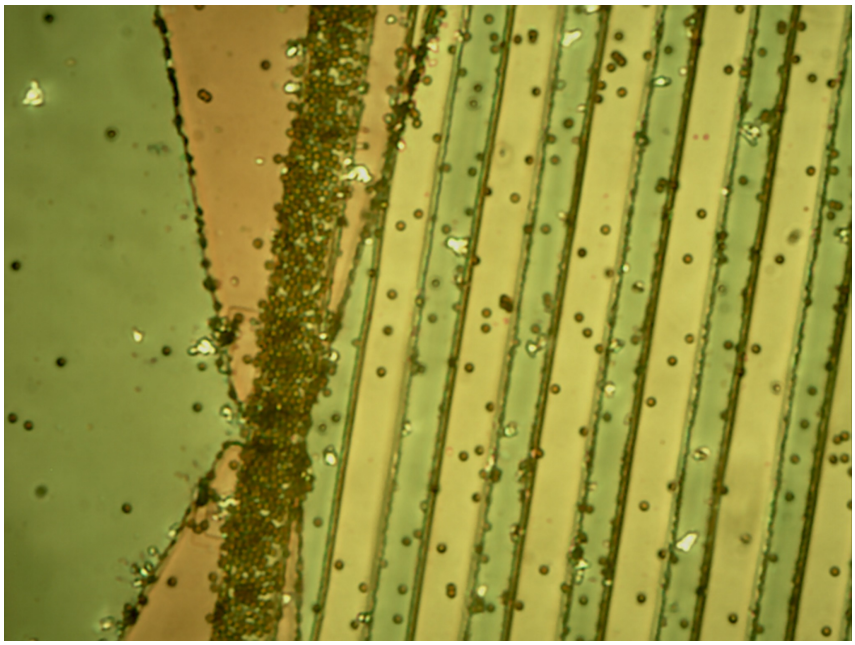

Figure 5.8.: Particles above the GMR sensor.

The output of the lock-in amplifier is depicted in figure 5.7. At the beginning a lot of particles are above the sensor (figure 5.8). After sucking out the particles, the voltage decreases by $\sim 1.2\ \mu$V.

Obviously the output voltage decreased significantly compared to the previous measurement in section 5.2 from 155.5 μV to 39.8 μV. The reason could be a decreased sensitivity of the GMR sensor due to electromigration. Therefore a second measurement was performed with Dynabeads 270, to be able to compare the different particles.

5.4. Measurement with the magnetophoresis-chip and Dynabeads 270 (reduced sensitivity)

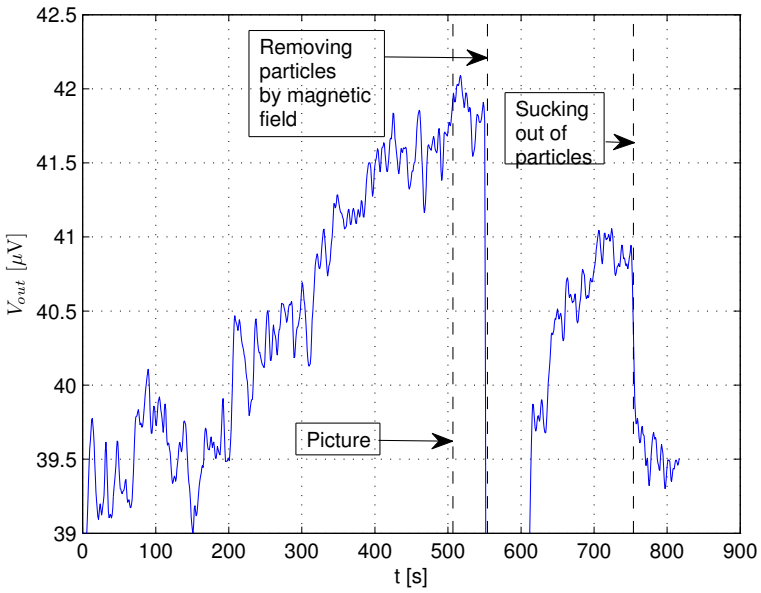

Figure 5.9.: Output at the lock-in amplifier over the time t. The output changes with the amount of particles above the sensor.

For the measurement 10 μl of "Dynabeads M-270 Carboxylic Acid" were suspended in 1 ml of deionised water. The particles have a diameter of $d = 2.8\ \mu$m and a susceptibility of $\chi = 1.0$.

For measuring the stray field of the particles a current of 10 mA with a frequency of 210 Hz was applied to the conductor and a current of 800 μA with a frequency of 2010 Hz was applied to the GMR sensor beneath the conductor. With a lock-in amplifier the voltage at the GMR sensor was measured at a frequency of 2220 Hz.

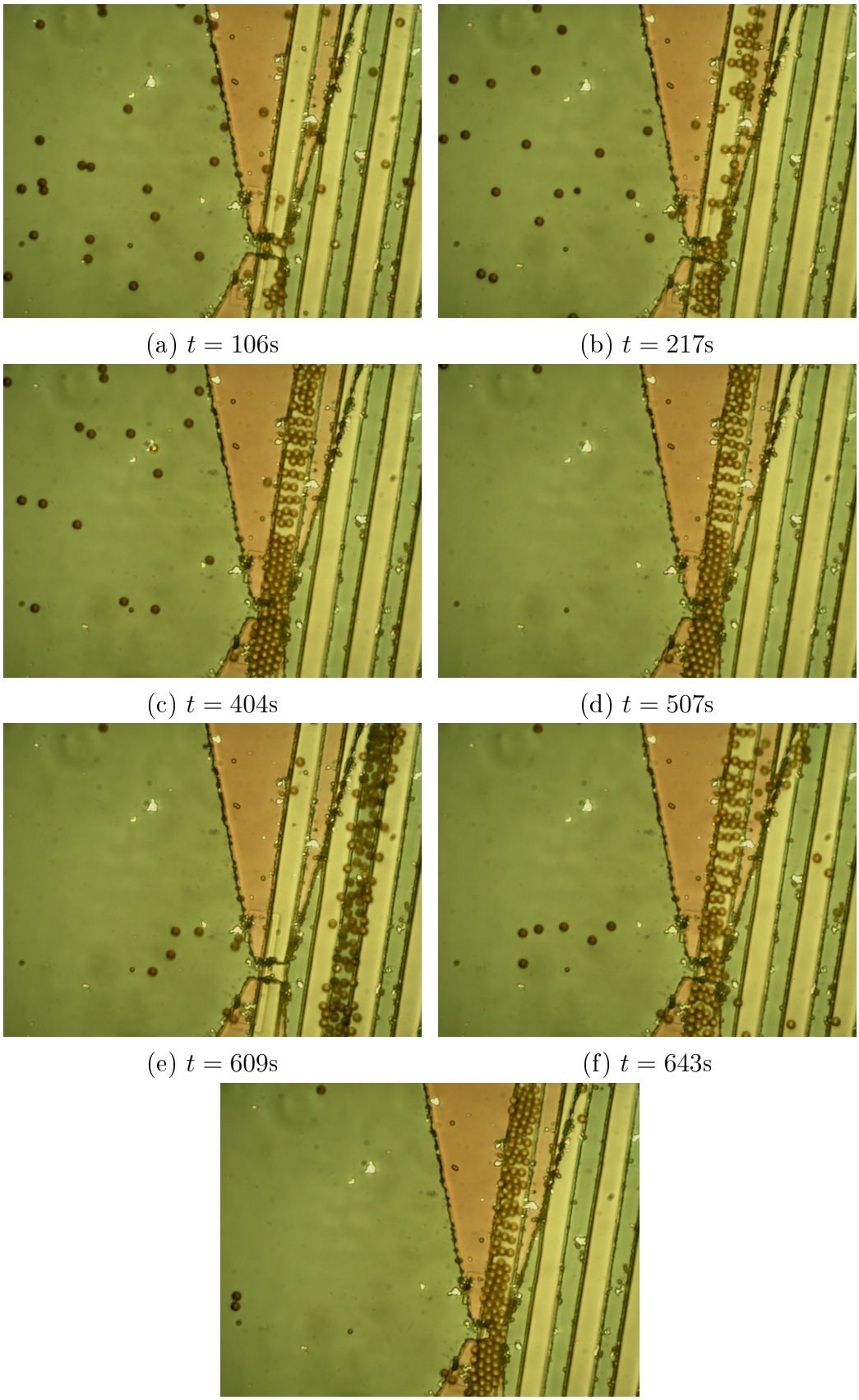

(a) $t = 106$s (b) $t = 217$s

(c) $t = 404$s (d) $t = 507$s

(e) $t = 609$s (f) $t = 643$s

(g) $t = 716$s

Figure 5.10.: Sensor with particles at different timepoints.

In figure 5.9 the output of the lock-in amplifier is depicted. The vertical lines indicate the timepoints when the pictures in figure 5.10 were made. First there were no particles above the sensor and the output voltage was ∼39.5 μV. More and more particles were attracted to the conductor and the voltage increased to ∼42 μV. Then the particles were removed by the magnetic field of the second conductor. After turning on the first conductor again, particles were attracted to the conductor and the voltage increased again. After washing away the particles at the end, the voltage decreased to the previous level of 39.5μV.

Thus a voltage change of $\sim 2.5\mu$V can be observed which is about twice as much as with Dynabeads MyOne. This is not surprising since with increased magnetic content the MPs have also a bigger magnetic moment.

6. Conclusion and Outlook

In this thesis two microfluidic devices for detecting magnetic particles (MPs) were presented. The device consists of a microfluidic channel, in which MPs are manipulated and trapped by a magnetic field gradient generated by current carrying conductors. A GMR sensor beneath a conductor was used to detect the MPs. Calculations have been performed to predict the output of the GMR sensor with particles above it. Several measurements were performed, in which MPs were detected to prove the concept.

The magnetophoresis-chip showed a much higher sensitivity to MPs than the microring-chip, because the area of the GMR sensor was much smaller and the sensitivity considerably higher. Considering the calculations also single MPs with a diameter ≥ 2.8 μm should be detectable with the magnetophoresis-chip. However, this possibility was not investigated during this thesis. Additional conductors to guide the MPs to the GMR sensor or a narrow microfluidic channel, which is just wide enough to cover the GMR sensor, with a controllable flow could facilitate the transport of single particles to the GMR sensor. Furthermore the particles rather moved to the middle of the conductor than being attracted to the edge, like expected from the calculations, thus the detection could be improved by fabricating the GMR sensor in the middle beneath the conductor.

With the microring-chip it was possible to attract particles from a wide area to the GMR sensor. From the output it could be possible to estimate the concentration, although it can not be determined exactly, because particles do not always land at the same position and the output varies with their position. For lower concentrations the design could be equipped with more than three microrings to cover an even wider area. The area of the sensor was not optimally utilised, since all particles were at the inner side of the microring. Making the sensor smaller by reducing the area on the outer side of the microring would result in a higher sensitivity. The Wheatstone bridge design of the microring-chip did not prove as necessary, since MPs could be detected very well without it. Maybe in situations with high temperature variations it could be useful.

As already stated in the Introduction, these chips could be used to detect biomolecules or biological cells by attaching them to the MPs. The next step could be to perform measurements with biological cells. Further those chips could be integrated into a Lab-on-a-chip for detecting biological cells, with a microfluidic structure to perform a mixing procedure to attach the MPs to the cells. The particles attached to a cell could be separated from the unattached particles by magnetophoresis [19] and then be detected with a

GMR sensor.

Appendix

Particle specifications

Dynabeads physical characteristics
Dynabeads are uniform, superparamagnetic, porous polystyrene spheres with an even dispersion of magnetic material throughout the bead. The magnetic material within the Dynabeads is a mixture of the two iron oxides maghemite (gamma-Fe_2O_3) and magnetite (Fe_30_4), which is encased in the bead matrix by an additional thin polymer shell. This prevents any iron leakage from the beads which could otherwise have a detrimental toxic effects on target cells, while at the same time providing a defined surface area for adsorption or conjugation of various biomolecules.

Dynabeads type	Diameter (µm)	Monodispersity		Specific surface area (m^2/ g DS)	Density (g DS/ cm^3)
		SD (µm)	CV (%)		
MyOne Dynabeads	1.0	0.02	2.0	8 - 16	1.8
M-270 Dynabeads	2.8	0.04 - 0.05	1.6 - 1.8	2 - 5	1.6
M-280 Dynabeads	2.8	0.04	1.6	4 - 8	1.4
M-450 Dynabeads	4.5	0.05	1.2	1 - 4	1.6

Table 1 Physical properties of Dynabeads (typical values)

Magnetic properties of Dynabeads
Due to the small size of the iron domains of the magnetic material in the matrix, Dynabeads are *superparamagnetic*. This means they will only exhibit magnetic properties when subjected to a magnetic field, and both *remanence* and *coercivity* equals zero. This can be seen from the magnetisation curves for the beads below.

MyOne, 1 micron Dynabeads

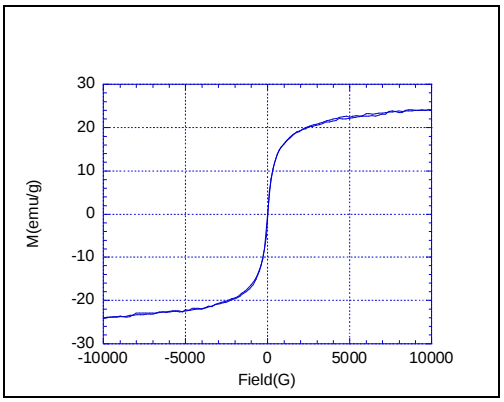

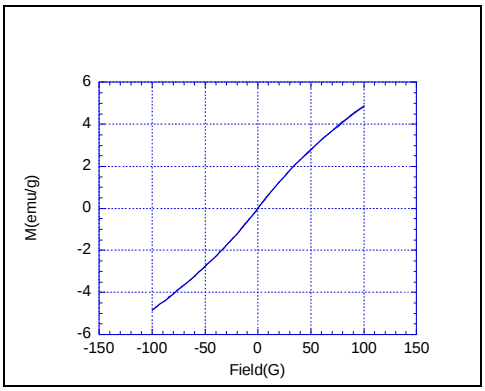

M-270/ M-280 Dynabeads (2.8 micron)

M-280 Dynabeads:

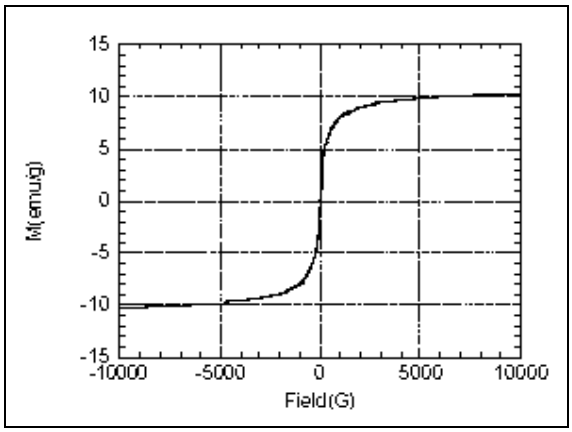

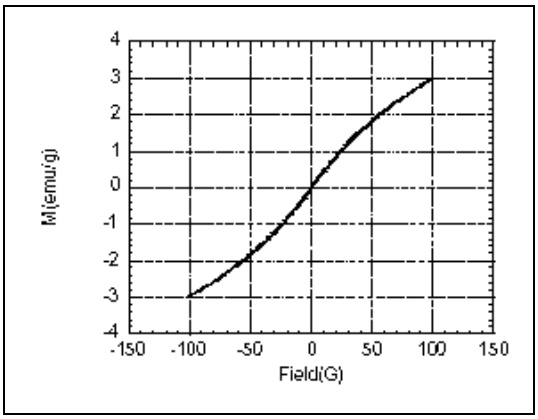

M-270 Dynabeads:

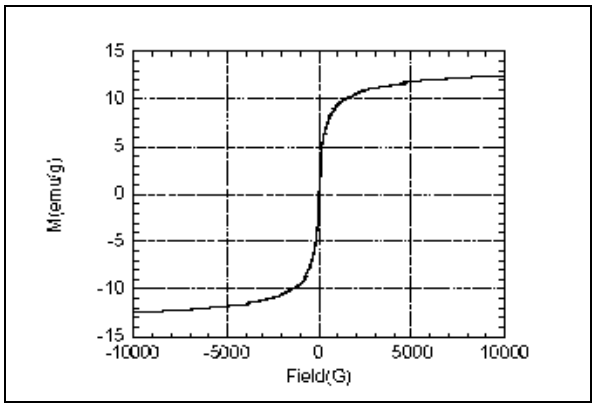

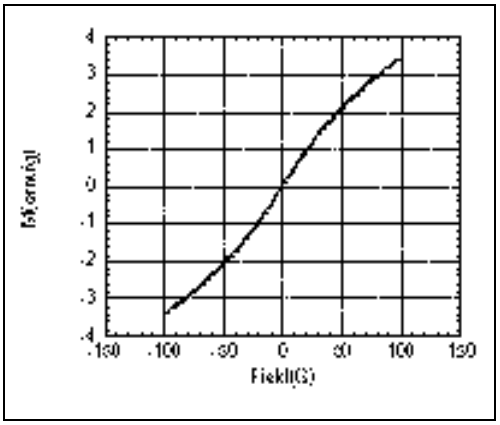

M-450 Dynabeads (4.5 micron)

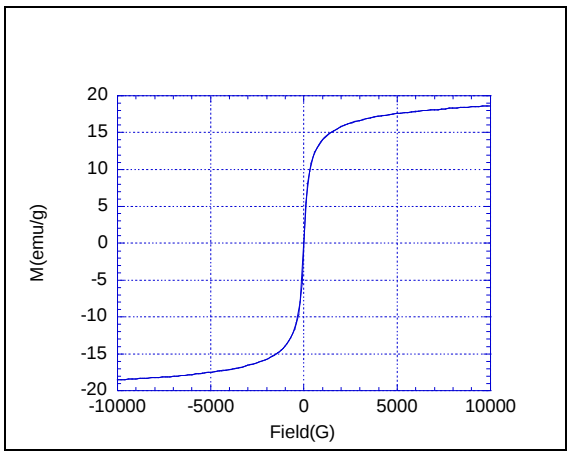

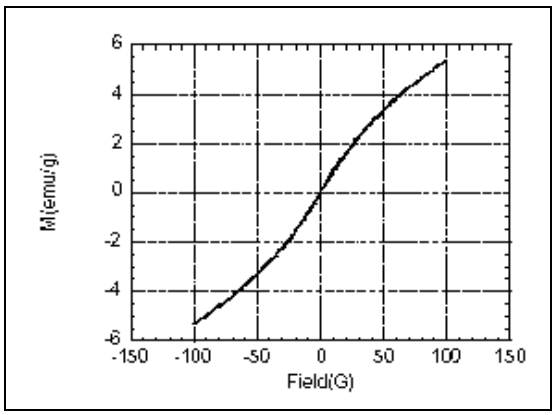

The *magnetic susceptibility* is used by Dynal as a measure of the beads magnetic properties. Magnetic susceptibility is measured by the oscillator method in the linear range of the magnetisation curve, and typical values for the different bead types are listed in table 2.

The magnetic force exerted on a bead – and hence the separation efficiency when exposed to a magnetic field – is dependant on the degree of magnetisation of the bead. The maximum magnetic field that may be generated by the beads is referred to as their *saturation magnetisation* (table 2). Due to the high magnetic content of Dynabeads their saturation magnetisation is high, which enables a quick and efficient separation even in viscous samples. Iron content in the beads are in the range 12% - 26%, depending on the bead type. This is further specified in table 2.

Dynabeads product	**Diam. (µm)**	**Magnetic Susceptibility[1] (dry substance)**		**Saturation Magnetisation[2] (kA/m)**		**Iron content (%, w/w dry substance)**
		m^3/kg (mass)	**Dimensionless (volume)**	**$A \cdot m^2/kg$ (mass)**	**kA/m (volume)**	
MyOne Dynabeads	1.0	$8 \cdot 10^{-4}$	1.4	24	43	26
M-270 Dynabeads	2.8	$6 \cdot 10^{-4}$	1.0	13	20	14
M-280 Dynabeads	2.8	$5 \cdot 10^{-4}$	0.7	10	14	12
M-450 Dynabeads	4.5	$10 \cdot 10^{-4}$	1.6	19	30	20

Table 2 Magnetic properties of Dynabeads (typical values)

List of Figures

List of Tables

Bibliography

[1] Martin A. M. Gijs, Frederic Lacharme, and Ulrike Lehmann. Microfluidic applications of magnetic particles for biological analysis and catalysis. *Chemical Reviews*, 110(3):1518–1563, 2010.

[2] J.C. Rife, M.M. Miller, P.E. Sheehan, C.R. Tamanaha, M. Tondra, and L.J. Whitman. Design and performance of gmr sensors for the detection of magnetic microbeads in biosensors. *Sensors and Actuators A: Physical*, 107(3):209 – 218, 2003.

[3] David R. Baselt, Gil U. Lee, Mohan Natesan, Steven W. Metzger, Paul E. Sheehan, and Richard J. Colton. A biosensor based on magnetoresistance technology. *Biosensors and Bioelectronics*, 13(7â8):731 – 739, 1998.

[4] V. K. Varadan, L. Chen, and J. Xie. *Design and Applications of Magnetic Nanomaterials, Nanosensors and Nanosystems*. John Wiley & Sons, 2008.

[5] Brian D. Plouffe, Laura H. Lewis, and Shashi K. Murthy. Computational design optimization for microfluidic magnetophoresis. *Biomicrofluidics*, 5(1), 2011.

[6] Franz Keplinger. *Advanced Materials*. 2011.

[7] Reinder Coehoorn. Novel magnetoelectronic materials and devices. 2003.

[8] E. Generalic. Laminar flow. Website. Available on: http://glossary.periodni.com/glossary.php?en=laminar+flow; visited on 28.08.2014.

[9] N.-T. Nguyen and S. T. Wereley. *Fundamentals and Applications of Microfluidics*. Artech House, Inc., 2002.

[10] Tabeling P. *Introduction to Microfluidics*. Oxford University Press, 2005.

[11] Adalbert Prechtl. *Vorlesungen über die Grundlagen der Elektrotechnik: Band 2*. SpringerWienNewYork, 2007.

[12] Eric Dennison. Off-axis field due to a current loop. Website. Available on: http://www.netdenizen.org/emagnet/offaxis/iloopoffaxis.htm;.

[13] I. Giouroudi, G. Kokkinis, C. Gooneratne, and J. Kosel. Microfluidic biosensing device for controlled trapping and detection of magnetic microparticles. In *Biomedical Engineering Conference (SBEC), 2013 29th Southern*, pages 1–2, May 2013.

[14] I. Giouroudi, C. Gooneratne, and G. Kokkinis. Controlled trapping and detection of magnetic particles by a magnetic microactuator and a giant magnetoresistance (gmr) sensor. In *Key Engineering Materials Vol. 605 (2014)*, pages 352–355, 2014.

[15] M. Stipsitz, G. Kokkinis, C. Gooneratne, J. Kosel, S. Cardoso, F. Cardoso, and Giouroudi I. Magnetic microfluidic platform for biomedical applications using magnetic nanoparticles. *accepted* Proc. 4th International Conference on Materials and Applications for Sensors and Transducers (IC-MAST), Bilbao, Spain, June 2014.

[16] Stanford Research Systems Inc. About lock-in amplifiers. Application note. Available on: http://www.thinksrs.com/downloads/PDFs/ApplicationNotes/AboutLIAs.pdf; visited on 11.09.2014.

[17] C.P. Gooneratne, I. Giouroudi, and J. Kosel. Microdevice with half-ring shaped gmr sensors for magnetic bead manipulation and detection. In *Advancement in Sensing Technology*, volume 1, pages 121–138. 2013.

[18] SK. Sia and GM. Whitesides. Microfluidic devices fabricated in poly(dimethylsiloxane) for biological studies. *Electrophoresis*, 24:3563–3576, 2003.

[19] Alexander Dangl. *Biosensing based on magnetically induced motion of magnetic microparticles*. Master Thesis, TU Wien, 2013.